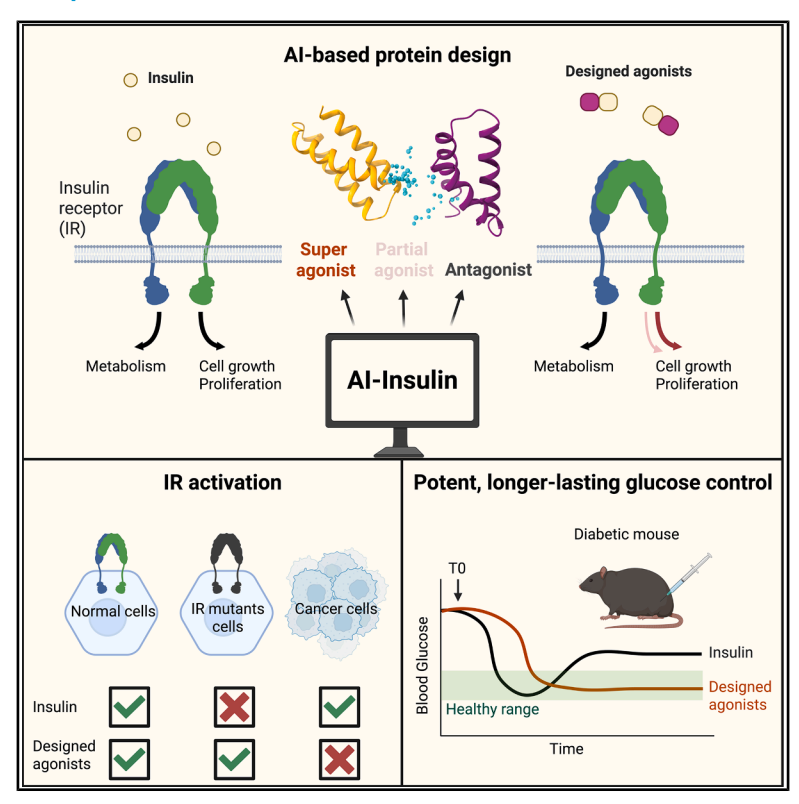
Tuning insulin receptor signaling using de novodesigned agonists

Graphical abstract



Highlights

- Computational design created insulin receptor (IR) agonists and antagonists
- Designed agonists stabilize distinct IR conformations and fine-tune signaling
- Designed agonists surpass insulin, prolong glucose lowering, and rescue mutant IRs
- Designed agonists activate IRs in normal cells but do not drive cancer cell proliferation

Authors

Xinru Wang, Sarah Cardoso, Kai Cai, ..., Eunhee Choi, Xiao-chen Bai, David Baker

Correspondence

xinruw7@uw.edu (X.W.), ec3477@cumc.columbia.edu (E.C.), xiaochen.bai@utsouthwestern.edu (X.-c.B.), dabaker@uw.edu (D.B.)

In brief

Wang, Cardoso, and Cai et al. design synthetic insulin receptor agonists that impose distinct receptor conformations, leading to modulated signaling. These agonists outperform insulin in metabolic control, remain active on disease-causing mutants, and reduce mitogenic responses, providing insight into how receptor conformations shape signaling outcomes and enabling safer insulin-like therapeutics.





Article

Tuning insulin receptor signaling using de novo-designed agonists

Xinru Wang,^{1,2,11,*} Sarah Cardoso,^{3,11} Kai Cai,^{4,11} Preetham Venkatesh,^{1,2,5} Albert Hung,³ Michelle Ng,³ Catherine Hall,³ Brian Coventry,^{1,2} David S. Lee,^{1,2,6} Rishabh Chowhan,^{1,2} Stacey Gerben,^{1,2} Jie Li,⁴ Weidong An,⁴ Mara Hon,³ Michael Gao,³ Ya-Cheng Liao,⁷ Domenico Accili,⁸ Eunhee Choi,^{3,12,*} Xiao-chen Bai,^{4,9,*} and David Baker^{1,2,10,*}

https://doi.org/10.1016/j.molcel.2025.09.020

SUMMARY

Insulin binding induces conformational changes in the insulin receptor (IR) that activate the intracellular kinase domain and the protein kinase B (AKT) and mitogen-activated protein kinase (MAPK) pathways, regulating metabolism and proliferation. We reasoned that designed agonists inducing different IR conformational changes might induce different downstream responses. We used *de novo* protein design to generate binders for individual IR extracellular domains and fused them in different orientations with different conformational flexibility. We obtained a series of synthetic IR agonists that elicit a wide range of receptor autophosphorylation, MAPK activation, trafficking, and proliferation responses. We identified designs more potent than insulin, causing longer-lasting glucose lowering *in vivo* and retaining activity on disease-causing IR mutants, while largely avoiding the cancer cell proliferation induced by insulin. Our findings shed light on how changes in IR conformation and dynamics translate into downstream signaling, and with further development, our synthetic agonists could have therapeutic utility for metabolic and proliferative diseases.

INTRODUCTION

The insulin receptor (IR) is a receptor tyrosine kinase (RTK) that plays an important role in metabolism, development, growth, and proliferation. The insulin-activated IR undergoes *trans*-autophosphorylation and phosphorylates a number of intracellular substrates, activating two major signaling pathways—the protein kinase B (AKT) pathway and the mitogen-activated protein kinase (MAPK)/extracellular-signal-regulated kinase (ERK) pathway. These phosphorylation cascades control trafficking events, transcription programs, glucose and lipid metabolism, and growth in different tissues and pathophysiological conditions. Dysregulation of IR signaling causes diseases including diabetes and cancer.

Unlike most other RTKs, which are monomeric and dimerize upon ligand binding, the IR is a preformed dimer composed of

two protomers covalently linked by disulfide bonds. $^{9-17}$ Structural studies have resolved the IR in both inactive and active states $^{18-25}$ (Figure 1A). Insulin binding occurs at two distinct extracellular sites: the primary site (site-1), located in the leucine-rich repeat 1 (L1)/C-terminal tail of the α -subunit (α -CT), and the secondary site (site-2), on the side of the F1 domain (Figures 1A and 1B). Ligand binding induces conformational rearrangements that decrease the distance between the intracellular kinase domains, enabling *trans*-autophosphorylation. It has been proposed that distinct ligand-bound conformations of the active receptor are critical for specifying downstream outputs. 20,21 However, because of the complexity of these large receptor-ligand assemblies and the structural similarity observed across ligands that elicit divergent biological effects, how extracellular conformational changes of the IR are coupled

¹Department of Biochemistry, University of Washington, Seattle, WA, USA

²Institute for Protein Design, University of Washington, Seattle, WA, USA

³Department of Pathology and Cell Biology, Vagelos College of Physicians and Surgeons, Columbia University, New York, NY, USA

⁴Department of Biophysics, University of Texas Southwestern Medical Center, Dallas, TX, USA

⁵Graduate Program in Biological Physics, Structure and Design, University of Washington, Seattle, WA, USA

⁶Department of Genome Sciences, University of Washington, Seattle, WA, USA

⁷Department of Biochemistry and Molecular Biophysics, The Taub Institute for Research on Alzheimer's Disease and the Aging Brain, Columbia University, New York, NY, USA

⁸Department of Medicine, Vagelos College of Physicians and Surgeons, Columbia University, New York, NY, USA

⁹Department of Cell Biology, University of Texas Southwestern Medical Center, Dallas, TX, USA

¹⁰Howard Hughes Medical Institute, University of Washington, Seattle, WA, USA

¹¹These authors contributed equally

¹²Lead contact

^{*}Correspondence: xinruw7@uw.edu (X.W.), ec3477@cumc.columbia.edu (E.C.), xiaochen.bai@utsouthwestern.edu (X.-c.B.), dabaker@uw.edu (D.B.)



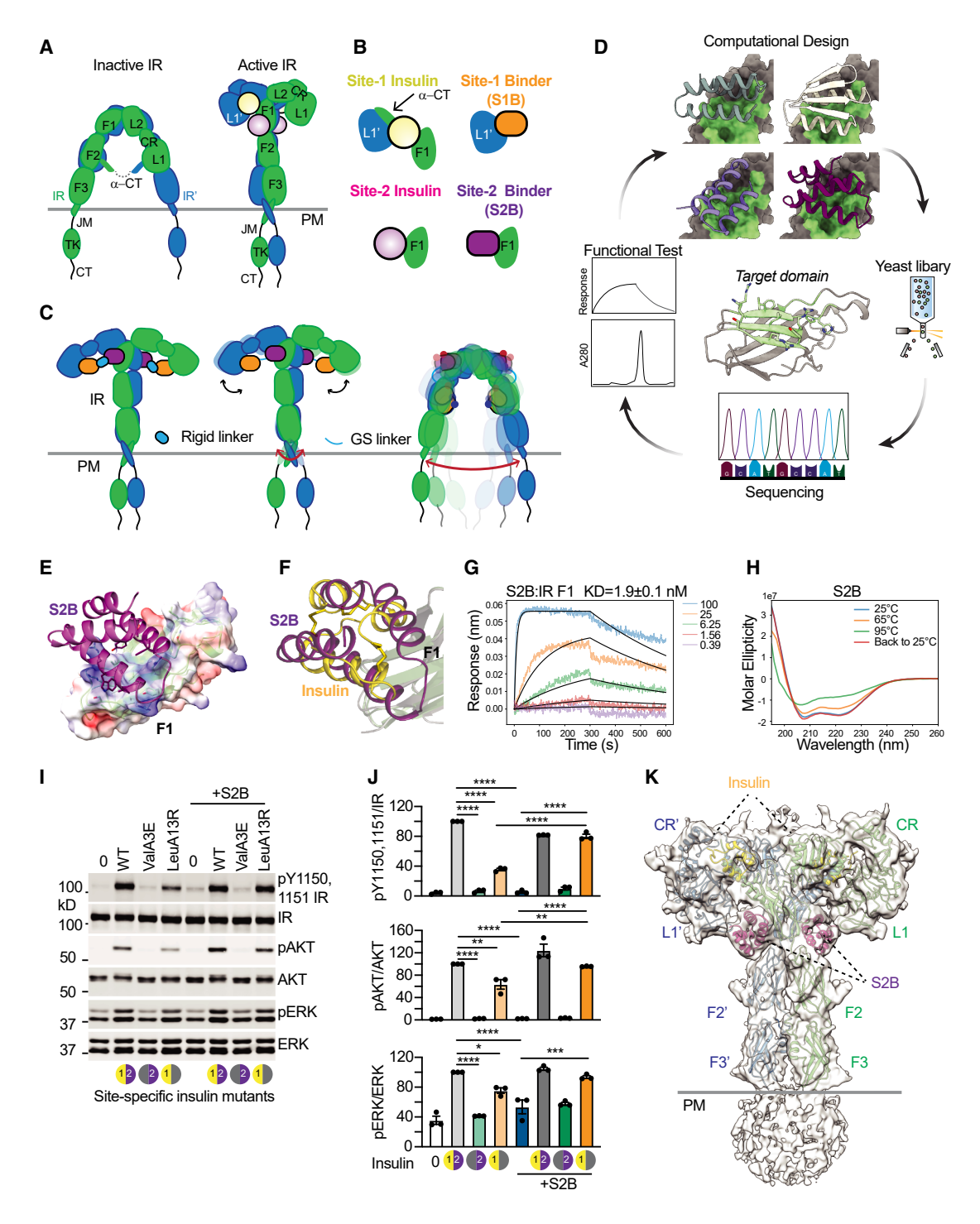


Figure 1. Design strategy for IR agonists

(A) Schematic of inactive apo-IR and insulin-bound active IR. Protomer 1 (green), protomer 2 (blue); leucine-rich repeats 1 and 2 (L1 and L2), cysteine-rich (CR), fibronectin type III-1, -2, and -3 (F1, F2, and F3), α-CT, juxtamembrane (JM), tyrosine kinase (TK), and CT domains shown. Domains of protomers 1 and 2 are labeled L1-TK and L1'-TK'. Site-1 insulins (yellow) and site-2 insulins (pink). PM, plasma membrane.

- (B) Tripartite interaction between insulin and IR L1', α-CT, and F1 (site-1) and insulin with IR F1 (site-2) (left), with target domains and designed binders (right).
- (C) Design strategy: RF of S1B/S2B fixes L1-F1 positions, while flexible linkers preserve receptor conformational flexibility.
- (D) Scheme of protein binder development workflow.
- (E) Model of S2B:IR F1 domain complex, with F1 domain as electrostatic surface and S2B as purple cartoons with key residues shown as sticks.

(legend continued on next page)



to intracellular signaling, trafficking, and biological outcomes is not well understood.

We reasoned that de novo protein design could provide a powerful approach to address this challenge.²⁶⁻²⁹ There are only a small number of natural ligands for any given receptor, and the changes in conformation and dynamics they elicit in the target receptor are not easily modulated. Antibody and nanobody engineering have been used to induce dimerization and activate dimerization-dependent receptors, 30,31 but achieving precise control over receptor conformational states remains a major hurdle. In contrast, protein design can, in principle, generate a wide range of ligands that bind to multiple domains in receptor extracellular regions and tune their signaling outputs. To probe the relationship between IR extracellular conformation and intracellular signaling, we set out to design proteins that modulate the conformational change of the extracellular domains (ECDs) of the IR and to determine the effect of these on the extent of induced IR autophosphorylation and downstream signaling (Figure 1C). Such designed IR agonists could also have therapeutic potential: although recombinant insulin and its analogs have been used to treat type 1 and type 2 diabetes for nearly a century, these treatments are not without limitations, including complications in manufacturing processes and storage, which could potentially be reduced for hyperstable, easyto-manufacture designed proteins. 32

RESULTS

We hypothesized that synthetic molecules engaging two insulinbinding sites in the IR-ECD, inducing conformational changes that reduce the distance between intracellular kinase domains, could activate IR signaling. To generate IR ligands, we used a two-step approach: first, we designed binders for the L1 and F1 domains of the IR (Figure 1B), and second, we fused them to bring together IR subunits in different arrangements (Figure 1C). Such ligands could release the autoinhibitory conformation of the IR by displacing the α -CT motif from L1 and stabilize the active conformation by fixing the L1-F1 orientation. By varying linker rigidity, we aimed to assess how conformational stability of the active state affects downstream signaling and trafficking (Figure 1C). Previously, a miniprotein binder was developed to target L1 using a Rosetta-based design²⁶ (we refer to this below as S1B). We therefore began by designing IR site-2 binders.

De novo design of IR site-2 binders

We designed site-2 binders targeting the outer side of the IR F1 domain in its inactive state (Figure 1D) using the Rosetta rotamer interaction field (RIF) dock²⁶ and Fast Design with a high-resolution cryo-electron microscopy (cryo-EM) model

(PDB: 6PXV). ^{18,26} Designs were filtered based on Rosetta metrics (ddg, sasa, and contact patch)²⁶ and DeepAccNet (pLDDT). ³³ From 11,452 designs, 17 bound the F1 domain in yeast display screens at 1 nM IR (Figures 1D, S1A, and S1B). After optimization, several binders with helical bundle or ferrodoxin folds had sub-nanomolar to nanomolar affinity for IR by biolayer interferometry (BLI; Figures 1E, 1F, and S1B). One design, referred to as S2B, bound F1 with a K_D of 1.9 nM (Figure 1G), far stronger than insulin (K_D of 21 μ M; Figure S1C), and remained stable at 95°C (Figure 1H), unlike insulin (Figure S1D).

We tested the effects of S2B on IR signaling. The IR exists as two isoforms: the short isoform IR-A and the long isoform IR-B.34 We treated double-knockout (DKO)-IR-B cells (IR/insulin-like growth factor-1 receptor [IGF1R] DKO preadipocytes expressing human IR-B) with insulin wild type (WT), insulin ValA3E (a site-1-binding-defective mutant), and insulin LeuA13R (a site-2-binding-defective mutant), in the presence and absence of S2B. S2B alone did not activate the IR (Figures 1I and 1J). Consistent with previous work, insulin ValA3E did not activate the IR, whereas insulin LeuA13R partially activated IR and downstream signaling (Figures 1I and 1J). Cotreatment with insulin site-1- and site-2-binding-defective mutants can activate the IR,²⁰ and similarly, cotreatment of S2B with the insulin site-2binding-defective mutant enhanced IR autophosphorylation (pY1150,1151 IR) and downstream signaling compared with either treatment alone (Figures 11 and 1J). Similar results were obtained in cells expressing mouse IR-A (Figures S1E and S1F).

To probe the mechanism, we determined a 6 Å cryo-EM structure of mouse IR with insulin and S2B (Figures 1K and S2). Two insulin and two S2B molecules bound the IR at site-1 and site-2, respectively, promoting the symmetric T-shaped conformation. Thus, S2B mimics site-2 insulin by inducing similar IR conformational changes. Together, these results demonstrate that although inactive on its own, S2B can synergize with site-1-only-binding insulin to activate both IR isoforms.

Design of site-1 and site-2 binder fusions

The primary conformational change induced by insulin binding is the rearrangement of the F1 domain (site-2) from one protomer and the L1 domain (site-1) of the other protomer (L1') in the IR-ECD, bringing kinase domains into proximity and stabilizing the active conformation. We next sought to link S2B (which binds F1) with S1B (which binds L1') to induce such conformational change (Figure 2A), breaking the autoinhibitory conformation and rearranging IR to activate the kinase domains (Figure 1C). To test this, we overlaid the designed S1B/L1' and S2B/F1 domain models onto the apo-IR (PDB: 4ZXB) and the active IR (PDB: 8DTL)³⁵ (Figure S3), and fusions were generated by linking the two domains with glycine-serine (GS) linkers

⁽F) Superposition of S2B:IR F1 domain and insulin:F1 complex (PDB: 6PXV), showing overlapping binding areas (S2B, purple; insulin, yellow) with distinct topology.

⁽G) BLI of S2B binding to the IR F1 domain; global kinetic fit shown.

⁽H) CD spectra of S2B.

⁽I) IR signaling in DKO-IR-B cells treated with 10 nM WT or site-specific insulin mutants with or without 100 nM S2B for 10 min.

⁽J) Quantification of the western blot data shown in (I). Mean \pm SEM. n = 3. Significance by two-tailed Student's t test.

⁽K) Cryo-EM model of insulin/S2B/mouse IR complex with two protomers (green and blue), insulin (yellow), and S2B (purple). Cryo-EM density shown as transparent surface.



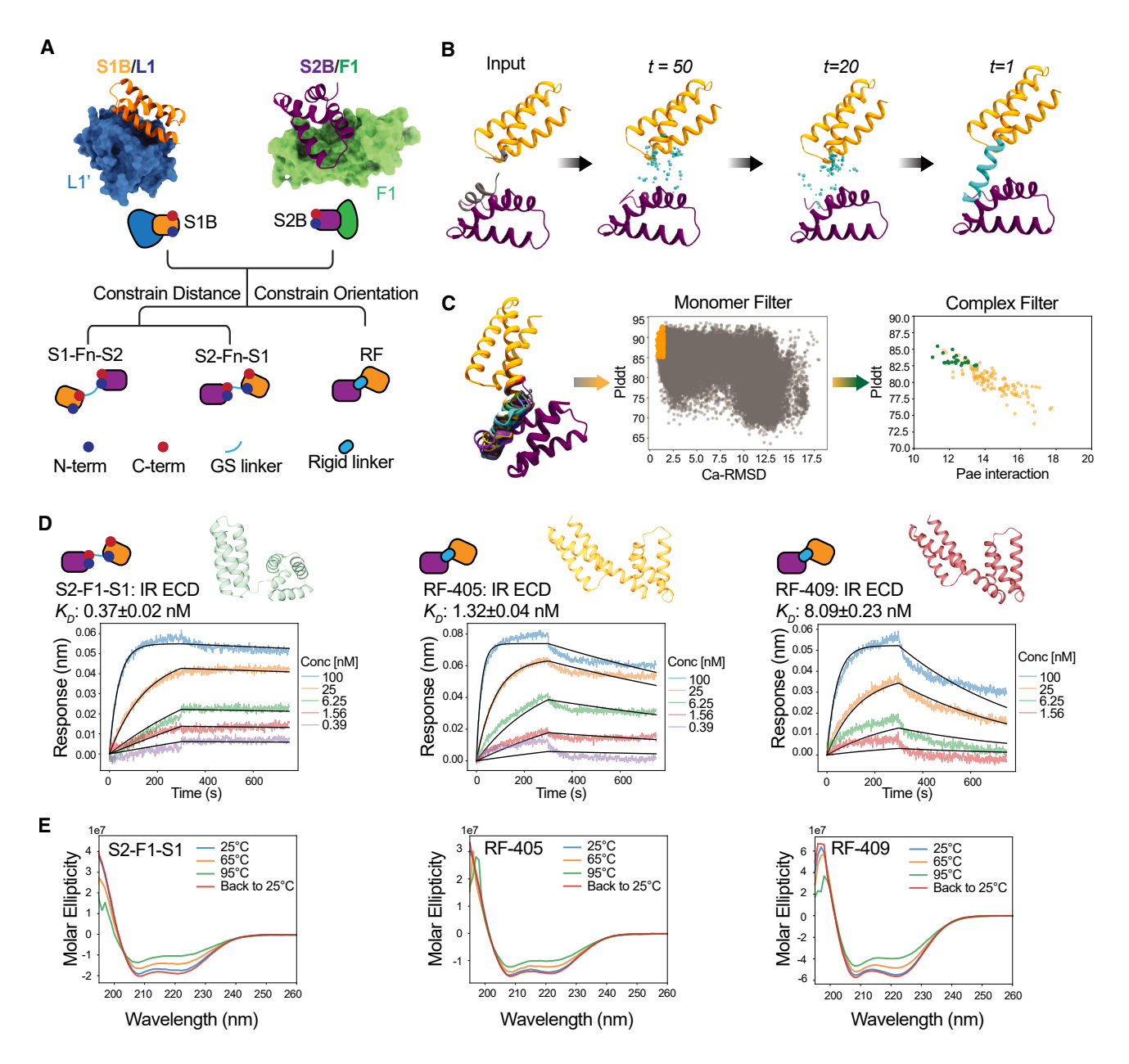


Figure 2. De novo design of IR agonists

(A) Design of site-1 and site-2 binder fusions using flexible GS linkers or RFs. The N terminus and C terminus of S1B or S2B are highlighted with blue and red dots, respectively.

- (B) Example RFdiffusion design trajectory for constructing a rigid linker between binding domains.
- (C) Sequences were generated for RFdiffusion backbones using ProteinMPNN, and the resulting designs were filtered using AlphaFold2 monomer (pLDDT score > 85, Cα-root-mean-square deviation [RMSD] < 1.5 Å) and design-target complex metrics.
- (D) Design models and BLI of S2-F1-S1, RF-405, and RF-409 binding to human IR-ECD. RF-405 and RF-409 are similar, with RF-409 more soluble and hence prioritized for *in vivo* use.
- (E) CD spectra of S2-F1-S1, RF-405, and RF-409 at various temperatures.

of varying lengths and orientations. In the composite structure, the S1B-C terminus to S2B-N terminus (S1B-S2B fusions; S1-Fn-S2) is $\sim\!18$ Å, whereas the S2B-C terminus to S1B N terminus (S2B-S1B fusions; S2-Fn-S1) is $\sim\!9$ Å (Figure S3). Thus, longer linkers (Fn; n, linker lengths = 3–11 residues) were used for S1-Fn-S2 and shorter ones (1–5 residues) for S2-Fn-

S1. The GS linker flexibility allows relative domain motion: shorter linkers reduce freedom, longer linkers increase flexibility and separation, while the shortest (n = 1) remains minimally mobile but not rigid.

To further constrain domain movement, we built rigid linkers using helices via RFdiffusion, generating S2-S1 fusions

Article



geometrically matched to insulin-binding sites L1′ and F1 in the active IR (PDB: 8DTL)^{28,35} (Figures 2B and 2C). The first helix of S1B and last helix of S2B were rebuilt, and redesigned with ProteinMPNN. From 32 sequences per backbone, 24 rigid fusion (RF) designs passed AF2³⁶ and Rosetta metrics²⁶ (pae interaction, pLDDT, ddg, and contact surface) and were tested for expression and solubility, binding, and IR activation.

Binding affinities were measured by BLI against IR-ECD. The rigidly linked binders RF-405 and RF-409 bound with K_D of 1.3 and 8.1 nM, respectively (Figure 2D). The flexibly linked fusion design, S2-F1-S1, bound with a K_D of 0.37 nM. All were specific, with no detectable binding of IGF1R, a homologous RTK that can be activated by insulin^{37–40} (Figure S1G). Circular dichroism (CD) studies showed that both flexible and rigid fusion constructs were hyper-thermostable (Figure 2E).

Characterization of synthetic agonists

We next tested the effects of the fusion constructs on IR activation and downstream AKT and ERK signaling (Figure 3A). The flexibly linked S1-S2 fusion (S1-Fn-S2) increased levels of IR autophosphorylation (pY1150,1151) to about 20% of that in insulintreated cells but did not increase pAKT or pERK levels (Figures 3B, 3C, and S4A). In the presence of insulin, S1-F8-S2 functioned as an antagonist, inhibiting insulin-dependent IR activation (Figures 3C-3E and S4B-S4D) and cell proliferation (Figure S4E).

In contrast to the S1-S2 fusion, the flexibly linked S2-Fn-S1 constructs functioned as partial (biased) agonists, whereas the rigidly linked RF-405 and RF-409 were full insulin mimics (balanced agonists; Figures 3B, 3C, and S4A). RF-405 and RF-409 elicited IR autophosphorylation (pY1150,1151 IR), pAKT, and pERK levels similar to insulin. In contrast, S2-Fn-S1 constructs increased pY1150,1151 IR and pAKT levels, but pERK levels were only 40% of those in insulin-treated cells (Figures 3B, 3C, and S4A; increasing the linker length reduces IR autophosphorylation). Although having comparable binding affinity (Figure 2D), the increased flexibility of S2-Fn-S1 compared with the rigidity of RF-405 and RF-409 appears to compromise balanced signaling.

We analyzed levels of pY1150,1151 IR, pAKT, and pERK over a wide range of ligand concentrations in cells (Figures 3F, S4F, and S5A). RF-405 and RF-409 potently activated both pAKT and pERK levels, similar to insulin, while S2-F1-S1 and S2-F5-S1 primarily activated pAKT, again indicating partial agonism. S2-F5-F1, which has a longer flexible linker, was significantly less effective at increasing pERK levels compared with S2-F1-S1 (Figures 3F, S4F, and S5A). A similar signaling pattern was also observed with the single-chain peptide S597. 35,41,42

Designed agonists modulate IR autophosphorylation, trafficking, and proliferation

When insulin activates the IR, several tyrosine residues in the juxtamembrane (e.g., Y960), kinase (e.g., Y1146, Y1150, and Y1151), and CT domains (e.g., Y1316 and Y1322) undergo *trans*-autophosphorylation (Figure 4A). These phosphorylation sites are crucial for recruiting downstream substrates. ^{1,43} To determine whether the observed pAKT and pERK activation patterns result from differential phosphorylation across these sites,

we measured the IR phosphorylation levels at these three intracellular sites. RF-405 increased autophosphorylation at all sites more than insulin (Figures 4B–4F, S4F, and S5B). Although S2-F1-S1 increased pY1150,1151 levels more than insulin (Figures 3F and S4F), phosphorylation at Y960 and Y1146 was lower (Figures 4C, 4D, S4F, and S5B), and phosphorylation at Y1316 and Y1322 in the CT domain was only 50% of insulin (Figures 4E, 4F, S4F, and S5B), indicating partial agonism. S2-F3-S1 and S2-F5-S1, which have longer flexible linkers than S2-F1-S1, were significantly less effective than S2-F1-S1 at increasing IR autophosphorylation in the juxtamembrane and CT domains (Figures 4C–4F, S4F, and S5B). These results indicate that agonist dynamics and geometry can modulate the extent of IR autophosphorylation during activation.

We next determined the effect of designed agonists on the phosphorylation of IR substrate 1 (IRS1) and src homology and collagen protein (SHC), the best characterized proximal mediators of IR signaling (Figure 4A). IRS1 and SHC bind to phosphorylated tyrosine 960 (pY960) in the NPEY⁹⁶⁰ motif in the juxtamembrane domain of the activated IR. 44-46 SHC also directly interacts with the CT domain of the IR, where phosphorylation of the IR at Y1316 and Y1322 promotes the IR-SHC interaction. ⁴⁷ As a result, the IR phosphorylates multiple tyrosine residues on the recruited IRS1 and SHC, which serve as docking sites for downstream effectors; IRS1 primarily activates the AKT pathway, whereas SHC activates the MAPK pathway. To determine whether the observed differential extent of IR autophosphorylation controls the levels of IRS1 and SHC phosphorylation, we tested the effects of designed IR agonists on the phosphorylation of IRS1 and SHC. The rigidly linked fusion RF-409 increased phosphorylation of IRS1 and SHC, similar to insulin (Figures 4G, 4H, S4F, and S5C), while the flexibly linked fusions S2-F1-S1 and S2-F3-S1 were slightly less effective in increasing IRS1 phosphorylation (Figures 4G, 4H, S4F, and S5C), consistent with their reduced ability to induce phosphorylation of IR Y960 (Figure 4C). By contrast, S2-F1-S1 increased SHC phosphorylation by only 50% compared with insulin, and S2-F3-F1 failed to increase SHC phosphorylation (Figures 4H, S4F, and S5C).

The MAPK pathway regulates cell growth and proliferation. ⁴⁸ We next investigated how the differences in the extent of MAPK pathway (pERK levels) activation by our synthetic agonists translate to differences in cell proliferation. We compared the ability of the designed agonists and insulin to induce cell proliferation (Figure 4I). RF-405 and RF-409 induced cell proliferation at levels comparable to insulin. At 1 nM, cells treated with RF-405 and RF-409 showed a 2-fold increase in proliferation compared with insulin. This enhanced proliferation may reflect the higher potency of RF-405 and RF-409 in inducing IR autophosphorylation. S2-F1-S1, which induced lower pERK levels, still induced cell proliferation, whereas S2-F3-S1, which is more defective in MAPK pathway activation, did not.

The insulin-activated IR undergoes endocytosis that can terminate and redistribute IR signaling. ^{49,50} The MAPK pathway plays a crucial role in regulating IR endocytosis⁵¹ (Figure 4A). To determine the effects of our synthetic agonists on IR endocytosis, we incubated S2-F1-S1, RF-409, or insulin with primary mouse hepatocytes and analyzed cell-surface IR and total IR levels. RF-409 and insulin, but not S2-F1-S1, significantly



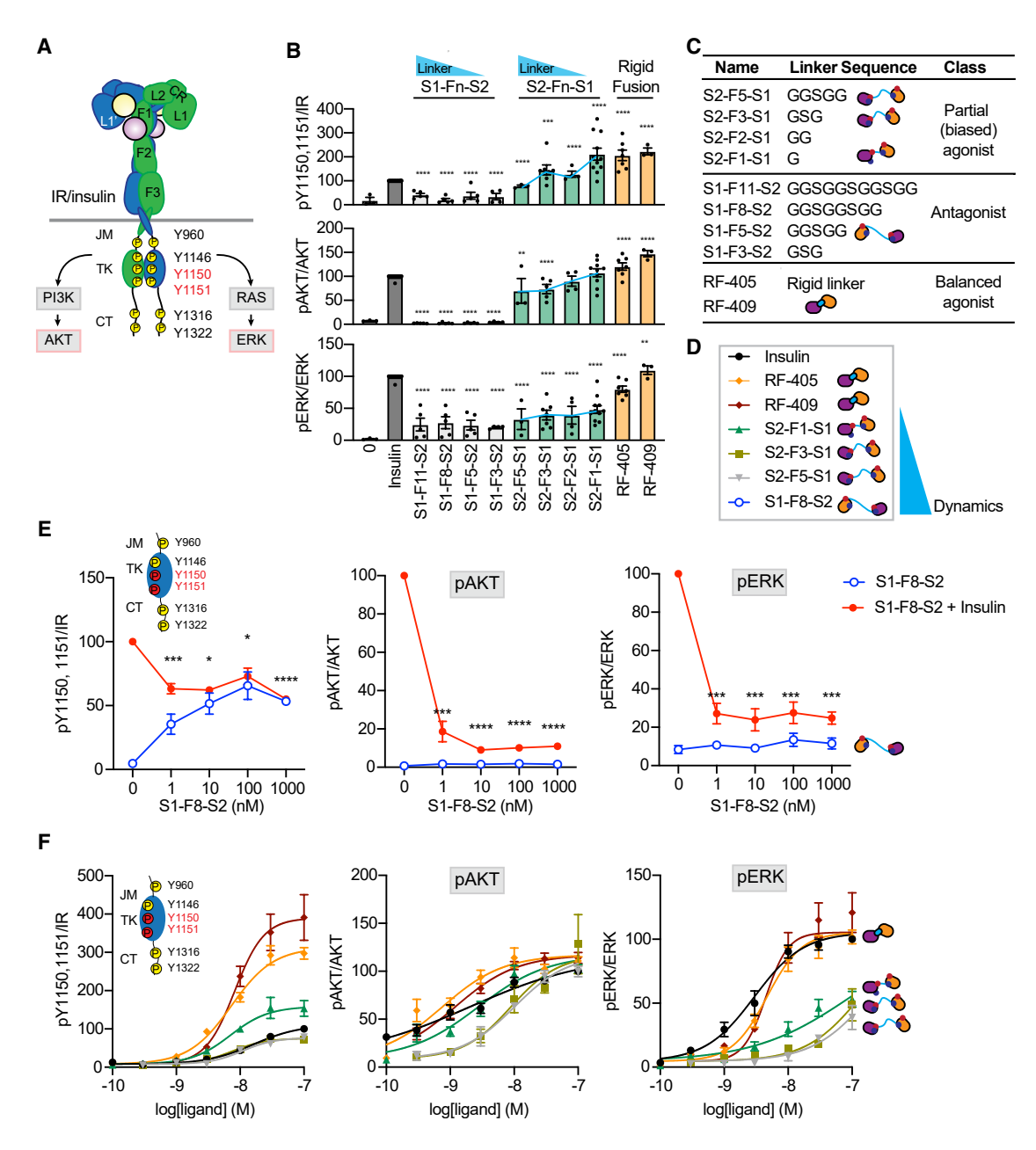


Figure 3. Differences in designed binder construct orientation and flexibility lead to differences in IR signaling

(A) Insulin triggers IR trans-autophosphorylation at multiple tyrosine residues in intracellular domains, activating two signaling pathways.

- (B) IR signaling in DKO-IR-B cells after 10 min with 10 nM ligands. Mean \pm SEM. $n \ge 3$. Significance by two-tailed Student's t test vs. insulin. **p < 0.001, ***p < 0.001, ***p < 0.0001.
- (C) Linker sequences of flexibly linked ligands and summary of three designed binder classes.
- (D) Legends for (E) and (F).
- (E) IR signaling in DKO-IR-B cells with insulin and S1-F8-S2. Cells were pretreated with S1-F8-S2 (1 h) and then 10 nM insulin (10 min). Mean \pm SEM. $n \ge 3$. Significance by two-way ANOVA. *p < 0.05, ***p < 0.001, ****p < 0.001.
- (F) IR signaling in C2C12-IR cells after 10 min ligand treatment, fit by nonlinear regression. Mean \pm SEM. $n \geq 3$.

reduced cell-surface IR levels (Figure 4J; none of the three molecules reduced total IR levels; Figure 4K). These data suggest that RF-409, like insulin, induces IR endocytosis, but S2-F1-S1 does not, supporting a role of MAPK activation in promoting IR endocytosis.

Taken together, these data show that modulating the linker flexibility and geometry of the designed IR agonists results in different signaling and trafficking outcomes. An equimolar mixture of unlinked S1B and S2B did not induce IR phosphorylation, pERK, or pAKT activation (Figures S1H and S1I),



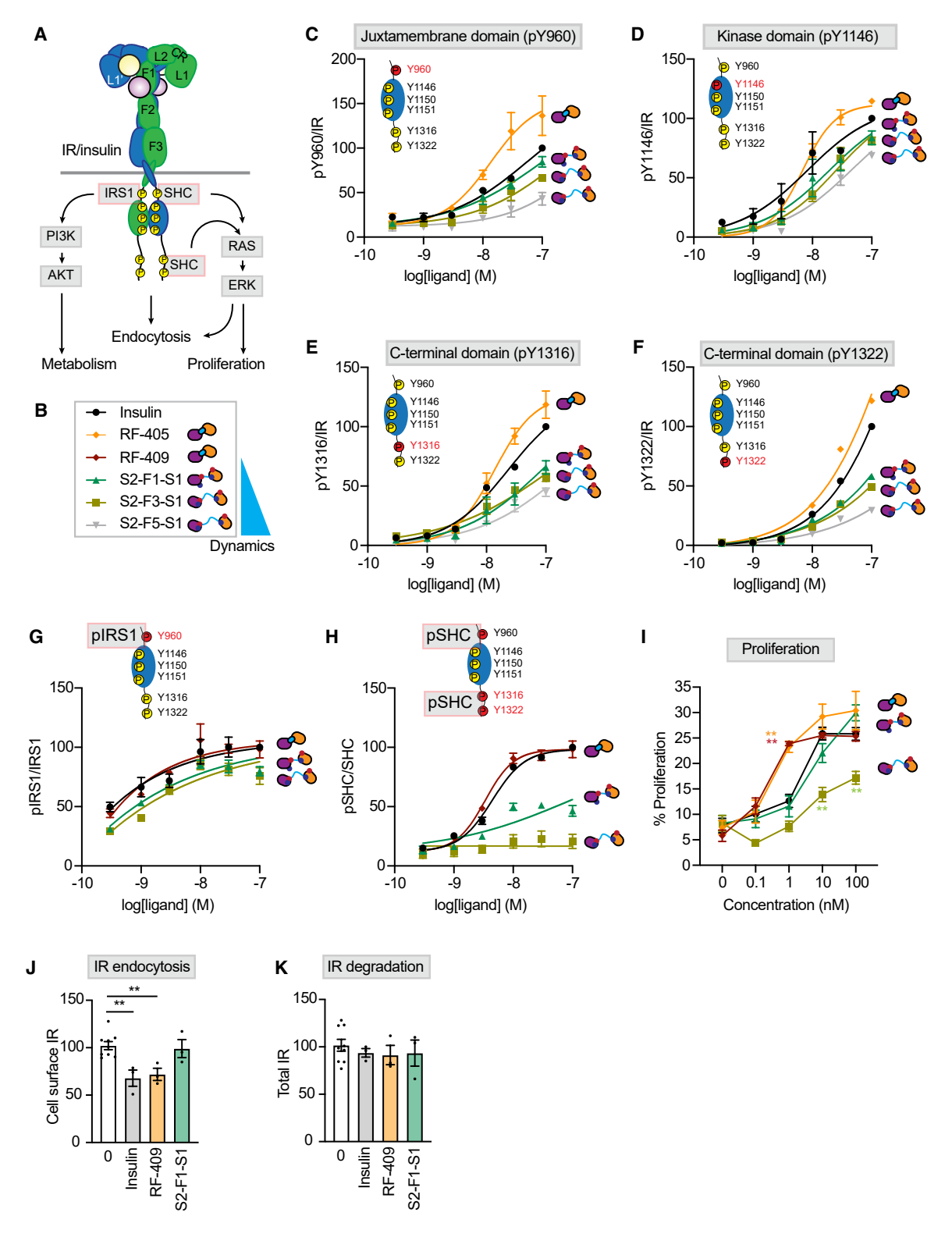


Figure 4. The linker dynamics of designed agonists control IR autophosphorylation and signaling outcomes
(A) Insulin activates IR autophosphorylation, recruiting IRS1 and SHC to trigger signaling. The MAPK pathway promotes IR endocytosis.
(B) Legends for (C)–(F).

(C–F) IR autophosphorylation in C2C12-IR cells after 10 min ligand stimulation, fit by nonlinear regression. Mean \pm SEM. $n \ge 3$. (G) IRS1 phosphorylation in C2C12-IR cells after 10 min ligand stimulation, fit by nonlinear regression. Mean \pm SEM. $n \ge 3$.

(legend continued on next page)



indicating that engagement of the two domains independently has no effect on IR activation. Rigid fusions of S1B and S2B induce insulin-like signaling and endocytosis, whereas allowing a wide range of conformations with flexible linkers results in partial agonism (reduced pERK signaling) and reduced endocytosis.

Cryo-EM complex structure determination

To determine the conformational changes induced by the designed fusion constructs, we determined cryo-EM structures of the RF-405/human IR (RF-405/IR) and S2-F1-S1/human IR (S2-F1-S1/IR) complexes at resolutions of 4 and 8 Å, respectively (Figures 5A-5D, S6, and S7; Table 1). The cryo-EM structure of the RF-405/IR complex exhibits an extended T-shaped architecture. A strong density between the two protomers at the top part of the IR was observed and unequivocally assigned to RF-405. The design models of S1B and S2B of the RF-405 fit well into the cryo-EM density as rigid bodies without further refinement; consistent with the models, the S1B binds the L1' domain of the IR (site-1) (Figure 5E), while the S2B contacts a side surface of the F1 domain of the adjacent IR protomer (site-2) (Figure 5F). S1B and S2B of RF-405 are linked through a continuous α -helix, as predicted in the design model (Figures 5A, 5B, and S6J). Both site-1 and site-2 interfaces involve both hydrophobic and electrostatic interactions, and Trp65 of RF-405 is sandwiched between the S1B and S2B components, enhancing the rigidity of the design (Figure 5G). The α-CT motif is displaced from the L1 domain upon the binding of the S1B of RF-405. RF-405 crosslinks the two IR protomers by simultaneously contacting site-1 and site-2, thereby stabilizing the extended T-shaped active conformation (Figures 5A and 5B). This conformation is similar to that induced by S597, 35 suggesting that the designed binders and S597 induce similar conformational changes to promote receptor activation.

The cryo-EM structure of S2-F1-S1 in complex with the IR was resolved at a lower resolution than the RF-405/IR complex: the flexibility of S2-F1-S1 likely translates to increased flexibility of the complex relative to the rigid RF-405 (Figures 5C, 5D, and S6H). The structure of the S2-F1-S1/IR complex has a similar extended T-shape to that of the RF-405/IR complex (Figures 5C and 5D). S1B and S2B of S2-F1-S1 are linked by a short, flexible loop (Figure 5H); superimposition of the bound S2-F1-S1 and RF-405 revealed that, due to the rigid linkage, the distance between the S1B and S2B domains of RF-405 is shorter than that of S2-F1-S1 (Figure 5H). The compact conformation of RF-405 allows its S1B component to simultaneously contact the L1' domain of one protomer and a loop in the top region of the F1 domain of the other protomer, further increasing the stability of the ECDs of IRs in the active state.

We next attempted to determine the cryo-EM structures of the antagonist S1-F8-S2/human IR (S1-F8-S2/IR) complexes (Figure S6K). Unlike S2B-S1B fusion constructs, 2D class aver-

aging of S1-F8-S2/IR revealed a high degree of conformational heterogeneity, and no stable active IR conformation was observed. Even though individual domains could be identified in a subset of 2D class averages, no high-resolution features were apparent (such as clearly identifiable secondary structural elements). These data suggest that the S1-F8-S2/IR complex samples a greater range of conformations than the S2-F1-S1 and RF-405 complexes. S1-F8-S2 may disrupt the autoinhibitory conformation of the IR but not stabilize the IR in an active conformation, consistent with its inability to activate IR and downstream signaling (Figure 3B) while antagonizing native insulin signaling (Figure 3E).

Comparison of designed agonists with native insulin

Our fusion constructs and insulin make different sets of contacts with the IR. Site-1 insulin interacts with both the L1' domain and α -CT motif, whereas S1B binds solely to the L1' domain (Figures 6A and 6B). To test the importance of each binding site to IR activation, we introduced mutations in the L1 domain (F64A, F88A, F89A, and F96A) that disrupt most insulin-L1 interactions but remove only a subset of contacts with the designed agonists (Figures 6C and S8A; the designs bury a substantially larger surface area on L1 compared with insulin-1,481.8 vs. 793.1 Å²). The F64A, F88A, F89A, F96A, F64A/F96A, and F88A/F89A mutants showed markedly reduced insulin-dependent IR activation (Figures 6C and S8A). In contrast, our designed agonists activated the IR F64A, F88A, F89A, F96A, and F64A/F96A mutants, suggesting that their larger site-1 interface compensates for the affinity reduction caused by the mutations. The F88A/F89A mutant compromised S2-F1-S1 signaling more than RF-405 signaling, suggesting that even though the rigidly linked and flexibly linked binders induce a similar T-shape, differences in structural dynamics and/or receptor-binding kinetics induce different mutation sensitivities.

To evaluate the role of the site-2 interface in IR activation, we introduced the K484E and L552A mutations (Figures 6D, 6E, and S8A). Insulin and S2-F1-S1 could not activate the IR K484E/L552A mutants, supporting the importance of the site-2 interface for IR activation.

Insulin generates intra- and inter-domain contacts that stabilize the active IR state. 18 Arg345 in the L2 domain and Glu697 in the $\alpha\text{-CT}$ form a salt bridge in the insulin-induced, compact T-shaped IR, and the R345A mutant is insulin resistant. We found that, unlike insulin, S2-F1-S1 and RF-405 were able to fully activate the IR R345A mutants (Figures 6E and S8A). Activation of the IR by the designed agonists is evidently less dependent on this Arg-Glu salt bridge, and the binding energy of the designed agonists is sufficient to overcome the loss of internal stabilization within the active state.

Mutations in the insulin-binding sites of the IR cause rare but severe insulin-resistance syndromes, such as Donohue syndrome and Rabson-Mendenhall syndrome. 52–54 Patients produce insulin

⁽H) SHC phosphorylation in C2C12-IR cells after 10 min ligand stimulation, fit by nonlinear regression. Mean \pm SEM. $n \ge 3$.

⁽I) Cell proliferation in C2C12-IR cells after 24 h ligand stimulation. Mean \pm SEM. $n \ge 3$. Significance by two-way ANOVA. p vs. insulin. **p < 0.01.

⁽J) Surface IR levels at 30 min after 100 nM ligand treatment in primary mouse hepatocytes. Mean \pm SEM. n = 3. Significance by two-tailed Student's t test. p vs. insulin. **p < 0.01.

⁽K) Total IR levels at 30 min after 100 nM ligand treatment in primary mouse hepatocytes. Mean \pm SEM. n = 3.



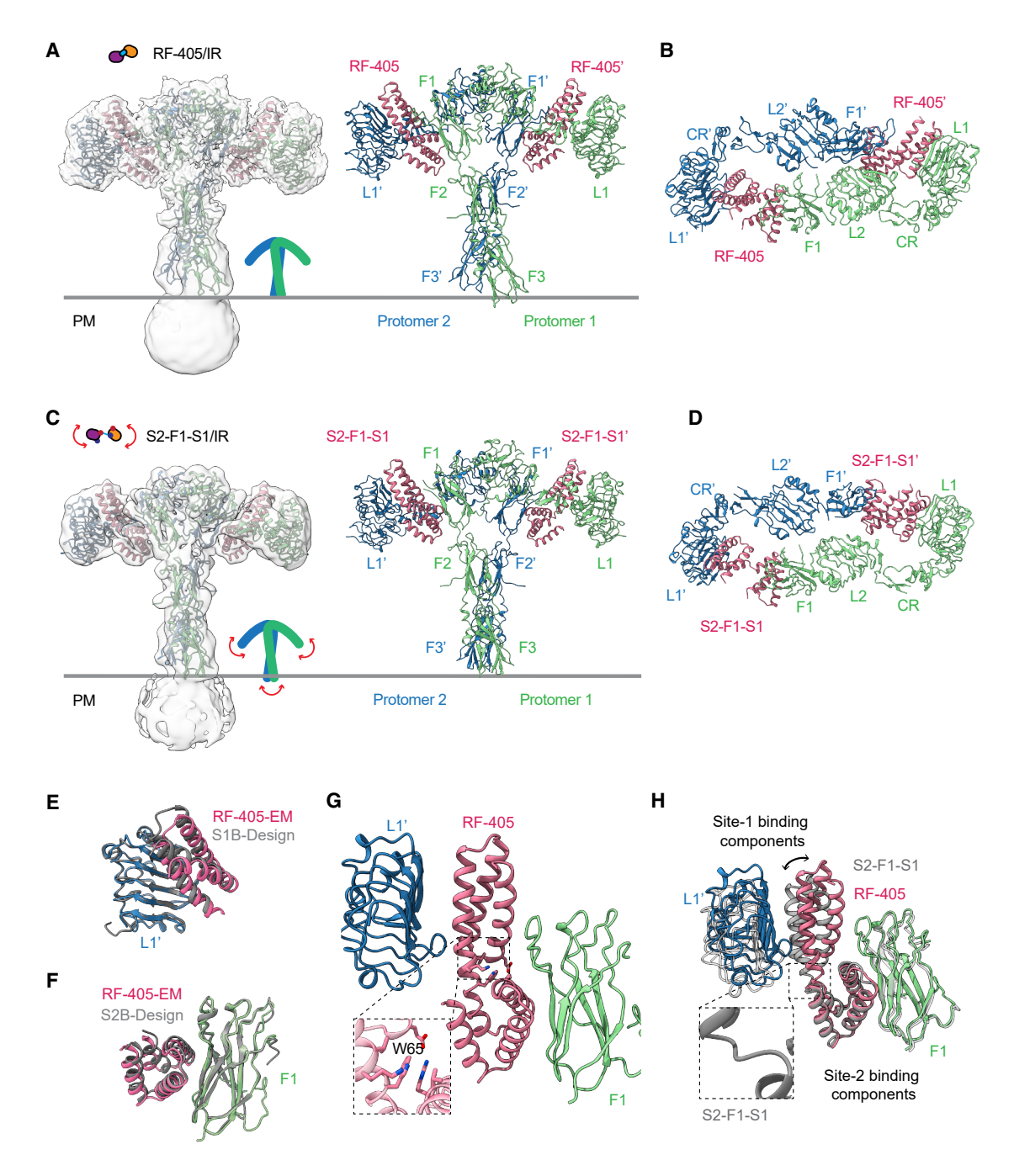


Figure 5. Cryo-EM structures of RF-405/IR and S2-F1-S1/IR complexes

- (A) Cryo-EM model of RF-405/human IR complex showing two protomers (green and blue), RF-405 (pink), and cryo-EM density as a transparent surface.
- (B) Top view of RF-405/human IR complex structure. The designed bindings of the L1 and F1 domains in each protomer are labeled.
- (C) Cryo-EM model of S2-F1-S1/human IR complex showing two protomers (green and blue), S2-F1-S1 (pink), and cryo-EM density as a transparent surface.
- (D) Top view of S2-F1-S1/human IR complex structure. The designed bindings of the L1 and F1 domains in each protomer are labeled.
- (E) Close-up view of RF-405 (pink) binding at the L1 domain (blue), with the S1B/IR L1 domain model overlaid (gray; RMSD = 0.60 Å).
- (F) Close-up view of RF-405 (pink) binding at the F1 domain (green), with the S2B/IR F1 domain model overlaid (gray; RMSD = 0.89 Å).
- (G) RF-405 (pink) binds at the IR L1' (blue) and F1 (green) domains, with Trp65 sandwiched between the site-1 and site-2 binding components.
- (H) Overlay of S2-F1-S1 (gray) and RF-405 (pink), aligned with the site-2 binding component. The linker of S2-F1-S1 is highlighted.



Table 1. Cryo-EM data collection and structure refinement statistics			
Structure	Insulin/S2B/mIR; EMD-47043; PDB: 9DNN	RF-405/hIR; EMD-47031; PDB: 9DN6	S2-F1-S1/hIR; EMD-47041; PDB: 9DNI
Magnification	45,000	130,000	81,000
Voltage (kV)	200	300	300
Electron exposure (e ⁻ /Ų)	60	60	60
Defocus range (μm)	1.2–2.2	1.2–2.2	1.2-2.2
Pixel size (Å)	0.88	1.07	1.404
Symmetry imposed	C2	C2	C2
Initial particle images (no.)	977,361	6,472,223	3,914,786
Final particle images (no.)	10,481	66,409	23,881
Map resolution (Å)	6.1	4.0	8.2
Fourier shell correlation (FSC) threshold	0.143	0.143	0.143
Initial model used (PDB code)	6PXV	6PXV	6PXV
Model composition			
Non-hydrogen atoms	29,774	28,535	28,144
Protein residues	1,866	1,766	1,742
RMSDs			
Bond length (Å)	0.003	0.004	0.004
Bond angle (°)	0.718	0.678	0.676
Validation			
Molprobity score	2.5	2.24	2.49
Clashscore	27.22	13.18	26.9
Poor rotamers (%)	0	0.44	0
Ramachandran plot			
Favored (%)	89.05	87.46	89.01
Allowed (%)	10.9	12.14	10.87
Outliers (%)	0.05	0.4	0.12

normally but are unable to properly regulate glucose metabolism. We introduced disease-causing mutations in the L1 (R14W 55 and N15K 56), F1 (D496N 57 and D496K), and α -CT (D707A 58) domains of the IR at sites that do not contribute to interactions with the designed IR agonists (Figures 6F and S8B). As expected, insulin could not activate the R14W, N15K, D496K, and D707A IR mutants. In contrast, both S2-F1-S1 and RF-405 could activate these disease-causing mutants (Figures 6F and S8B). These results highlight the differences in the activation mechanisms of our designed agonists, which could be beneficial for patients with insulin-binding-deficient IR mutants.

High insulin levels are associated with an increased risk of cancer, particularly breast, pancreatic, and colon cancer. ^{59–64} We tested whether our designed agonists could activate IR signaling and promote proliferation in cancer cells. Insulin induced IR autophosphorylation (pY1150,1151), pAKT, and pERK in human breast cancer cells (MCF7), whereas RF-405 did not (Figures 6G and S8C). Moreover, while RF-405 greatly increased non-cancer cell proliferation (Figure 4I), it did not increase cancer cell proliferation (Figure 6H). These data suggest that our designed agonists may not activate the IR in some types of cancer cells.

IGF1R expression is elevated in many cancer cell types compared with normal cells, and prior studies have suggested

that the IR can form heterodimers with IGF1R (i.e., comprising one IR protomer and one IGF1R protomer). Given that our designed agonists do not interact with IGF1R, we hypothesized that RF-405 might be unable to engage and activate IR-IGF1R hybrid receptors present in cancer cells. To test this, we knocked out IGF1R in MCF7 cells and assessed IR activation following stimulation with insulin or RF-405. Notably, RF-405 activated IR in IGF1R KO MCF7 cells, in contrast to its inactivity in parental MCF7 cells (Figures 6G and S8D). Consistent with the signaling results, RF-405 promoted cell proliferation in the IGF1R KO MCF7 cells (Figure 6H). These data suggest that the presence of IGF1R—and thus the formation of IR-IGF1R hybrid receptors—may interfere with RF-405-mediated activation of the IR, further suggesting that our designs selectively activate IR signaling in non-cancer cells.

Designed agonists mimic insulin functions in vivo

We set out to investigate the function of our designed agonists *in vivo*. The IR structure and sequence are highly conserved between humans and mice. We first tested whether the designed agonists could activate IRs in mouse cells (Figures S9A and S9B). We isolated primary mouse hepatocytes and compared insulin- and designed agonist-induced IR signaling. In primary hepatocytes, RF-409 increased IR autophosphorylation



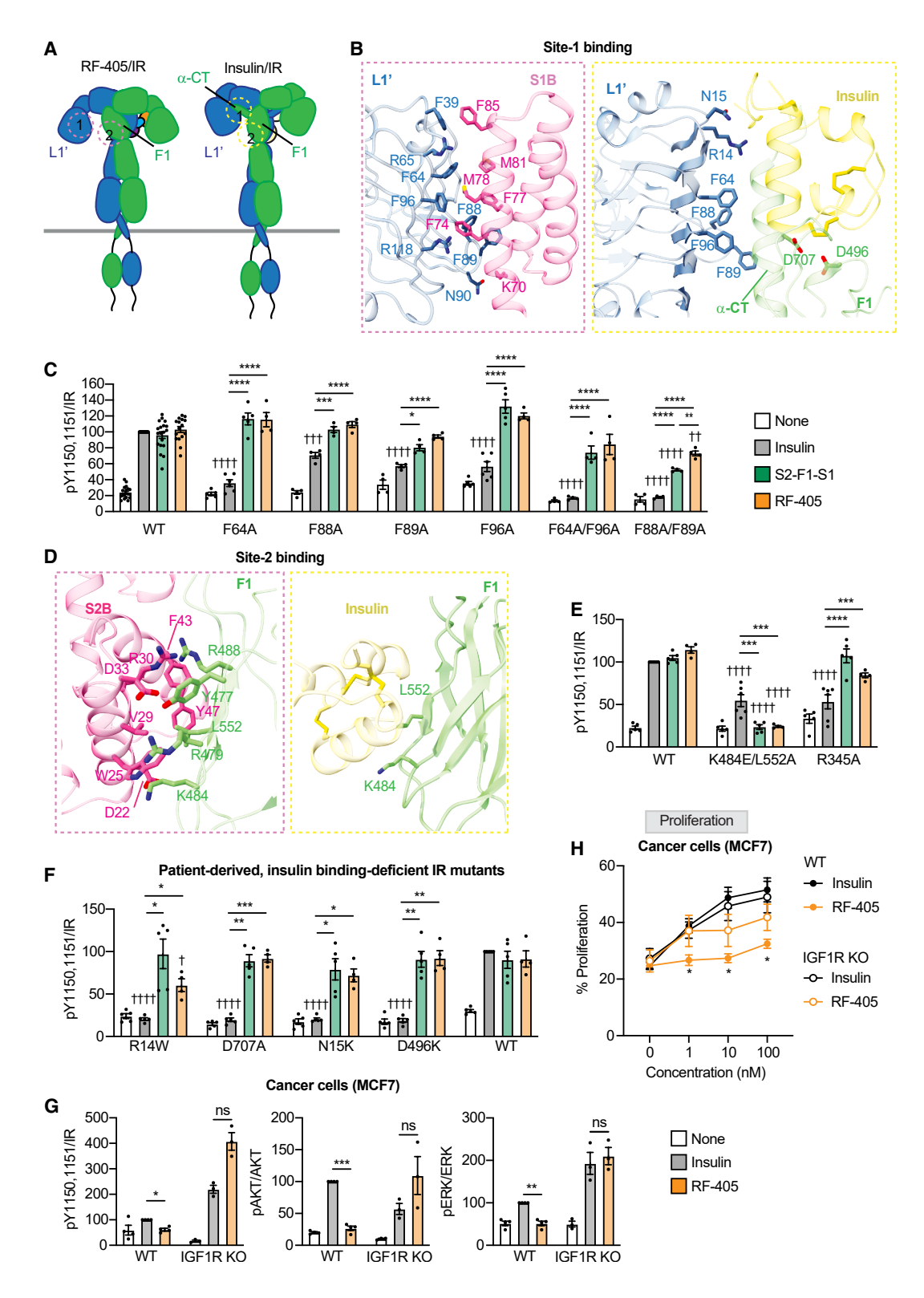


Figure 6. Designed IR agonists activate insulin-resistant IR mutants

(A) Schematic of RF-405/human IR (left) and insulin/human IR (right) complexes. Protomer 1 (green) and protomer 2 (blue); RF-405 (pink) and insulin (yellow) binding interfaces shown.

(legend continued on next page)



(pY1150,1151 IR) and pAKT, similar to insulin, while S2-F1-S1 induced pY1150,1151 IR, and pAKT less potently than RF-409. Due to the high basal levels of pERK in primary hepatocytes, even after insulin stimulation we did not observe significant increases in pERK.

We next compared IR signaling induced by S2-F1-S1 and RF-409 in metabolic tissues, including liver and skeletal muscle (Figures S9C and S9D). In both tissues, S2-F1-S1 was less effective in stimulating IR autophosphorylation, but it increased levels of pAKT to similar levels as RF-409. As in primary hepatocytes, mouse liver exhibited high basal levels of pERK, and we did not observe a significant difference between all tested molecules. In skeletal muscle, RF-409 significantly increased pERK levels, while S2-F1-S1 did not, confirming that the RF-409 is a full agonist, whereas S2-F1-S1 is a partial agonist *in vivo*.

To determine the metabolic effects of our designed agonists, we conducted an insulin tolerance test (ITT) in mice fed a normal diet (Figures 7A, 7B, S9E, and S9F). S2-F1-S1 reduced glucose levels in mice as effectively as insulin, while RF-409 was even more effective: with half the dose of RF-409, glucose levels decreased to the same level as with insulin. In addition, the designed agonists showed longer-lasting effects on glucose levels compared with insulin. Next, to determine the physiological effects of designed agonists under diabetic conditions, we conducted ITT in mice with diet-induced obesity, which have higher basal blood glucose levels. Similar to healthy mice, RF-409 and S2-F1-S1 slowly reduced glucose levels but exhibited prolonged glucose lowering effects compared with insulin. RF-409 was more effective at lowering glucose levels than S2-F1-S1 (Figures 7C and S9G). After a single injection of RF-409, mice maintained low glucose levels for 6 h, whereas in mice treated with insulin, glucose levels rose within 2 h (Figures 7D and S9H). Overall, our designed agonists effectively lower glucose levels in mice, RF-409 more potently than S2-F1-S1.

Origins of differences in signaling outcomes

It has long been thought that the IR-mediated AKT pathway controls metabolic function, while the MAPK pathway controls mitogenic function. However, molecular dissection of the two pathways has been hindered by the fact that the native ligand insulin activates both pathways. Our series of designed agonists provide insight into the mechanism of signaling through the IR and how receptor autophosphorylation is tied to downstream outcomes. As described in the following paragraphs, RF-405,

S2-F1-S1, and S2-F5-S1 all bind to the IR with high affinity but generate different signal transduction processes.

The rigid agonist RF-405 induces a highly ordered active conformation of the IR, which leads to efficient IR autophosphorylation in the juxtamembrane (pY960), tyrosine kinase (pY1150, pY1151), and CT (pY1316 and pY1322) domains (Figures 7E, 7F, and S4F). This results in strong activation of the AKT and MAPK pathways.

The intermediate flexibility agonist S2-F1-S1 induces a more dynamic conformation of the IR that is less able to autophosphorylate, particularly in regions distant from the kinase domain, such as the juxtamembrane and CT domains. As a result, the phosphorylation of SHC, an upstream regulator of the MAPK pathway, is reduced (Figures 7E, 7F, and S4F). Src Homology 2 Domain-Containing Protein Tyrosine Phosphatase 2 (SHP2),65 an activator of the MAPK pathway, docks on the IR following phosphorylation at the CT tyrosine sites and modulates IR signaling and endocytosis. 49,51,66-69 S2-F1-S1 is likely less effective in activating the MAPK pathway and IR endocytosis because it does not induce phosphorylation at these sites. S2-F1-S1 was less effective in controlling glucose levels in mice than the rigid agonists, suggesting an important role of the MAPK pathway in regulating metabolism (S2-F1-S1 does induce the AKT pathway).

The highly flexible agonists S2-F3-S1 and S2-F5-S1 showed even weaker MAPK pathway activation, while S1-F8-S2 failed to stabilize an active conformation and did not signal (Figures 7E and S4F). Instead, S1-F8-S2 disrupts the autoinhibitory state of the IR and functions as an antagonist by competing with insulin (Figure 7F).

DISCUSSION

Insulin activates the IR by engaging site-1 and site-2 individually, with distinct insulin molecules binding each site to stabilize a compact, active T state. In contrast, our designed agonists simultaneously engage site-1 and site-2 on each side of the receptor, in a manner more similar to how EGFs activates EGFRs, where each ligand binds to one side of the dimerized receptor. Our synthetic IR antagonists and agonists elicit diverse signaling outputs, with differences in IR autophosphorylation patterns, MAPK vs. AKT pathway activation, intracellular trafficking, and cell proliferation. These functional differences likely arise from differences in the conformation and dynamics of the

⁽B) Binding of RF-405 (left) and insulin (right, PDB: 6PXV) at the IR L1 domain. L1 domain shown as transparent blue cartoons, ligands as pink (RF-405) and yellow (insulin) cartoons, and key interacting residues as sticks.

⁽C) IR autophosphorylation in 293FT cells expressing WT or site-1 interface IR mutants after 10 min treatment with 10 nM ligands. Mean \pm SD. $n \ge 4$. Significance by two-way ANOVA; $\dagger p < 0.05$, $\dagger \dagger p < 0.05$, $\dagger \dagger p < 0.01$, $\dagger \dagger \dagger p < 0.001$, $\dagger \dagger \dagger p < 0.001$, $\dagger \dagger \dagger p < 0.001$ vs. WT IR (insulin treated).

⁽D) Binding of RF-405 (left) and insulin (right, PDB: 6PXV) at the IR F1 domain. F1 domain shown as transparent green cartoons, ligands as pink (RF-405) and yellow (insulin), and key interacting residues as sticks.

⁽E) IR autophosphorylation in 293FT cells expressing WT IR or the indicated mutants after 10 min treatment with 10 nM ligand. Mean \pm SD. $n \ge 4$. Significance by two-way ANOVA; $\dagger p < 0.05$, $\dagger \dagger p < 0.01$, $\dagger \dagger \dagger p < 0.001$, $\dagger \dagger \dagger p < 0.001$ vs. WT IR (insulin treated).

⁽F) IR autophosphorylation in 293FT cells expressing WT IR or disease-causing IR mutants after 10 min treatment with 10 nM ligands. Mean \pm SEM. $n \ge 4$. Significance by two-way ANOVA. $\dagger p < 0.05$, $\dagger \dagger p < 0.05$, $\dagger \dagger p < 0.01$, $\dagger \dagger \dagger p < 0.001$, $\dagger \dagger \dagger p < 0.001$, $\dagger \dagger \dagger p < 0.001$ vs. WT IR (insulin treated).

⁽G) IR signaling in MCF7 WT and IGF1R-KO cells treated with 10 nM insulin or RF-405 for 10 min. Mean \pm SEM. $n \ge 3$. Significance by two-tailed Student's t test. $t \ge 0.005$, $t \ge 0.001$. In significant.

⁽H) Cell proliferation in MCF7 WT and IGF1R KO cells treated with indicated ligand concentrations for 24 h. Mean ± SEM. n = 4. Significance by two-way ANOVA. *p < 0.05 vs. insulin-treated MCF7 WT.

Article



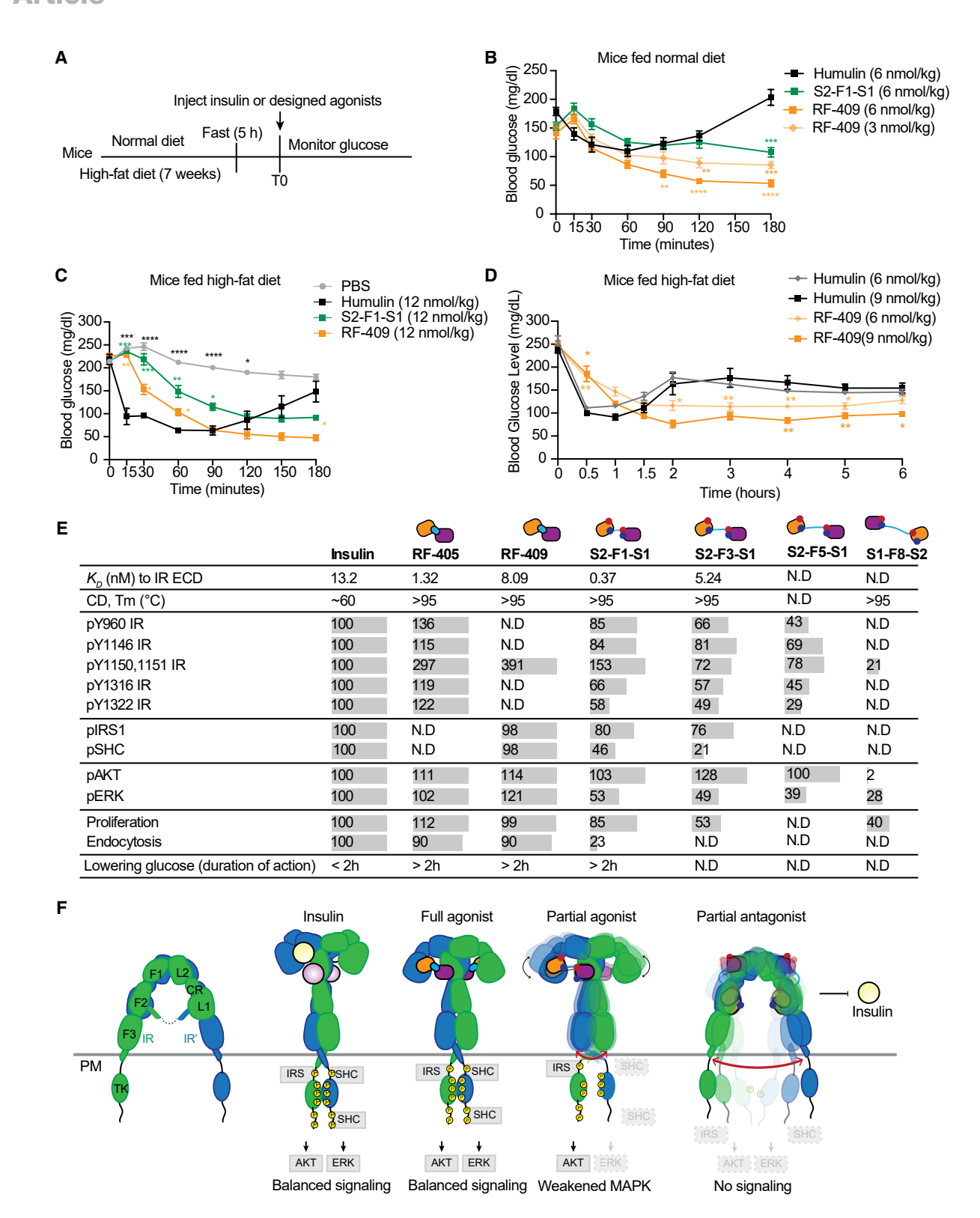


Figure 7. Designed IR agonists tune IR signaling and reduce glucose levels

(A) Schematic of mouse experiments with normal chow and high-fat diets (2- to 3-month-old male mice). (B) ITT in chow-fed mice. Mean \pm SEM; Humulin, n = 8; S2-F1-S1 and RF-409, n = 6. Significance by two-way ANOVA vs. Humulin; **p < 0.01, ****p < 0.001, ****p < 0.0001.

(legend continued on next page)



designed ligand-receptor complexes (Figure 7). Our designs range from antagonists that can simultaneously bind to both sites, but do not activate the receptor, to biased and full agonists. Cryo-EM characterization of the ligand-receptor complexes shows that the antagonist complex exhibits considerable conformational heterogeneity, while the biased and full agonists drive the receptor into a T-shaped active conformation similar to that observed with insulin. The biased agonist, like the antagonist, has the two domains flexibly rather than rigidly linked, and the receptor-cocomplex structure has somewhat lower resolution, perhaps indicating greater dynamics within the complex.

We can attribute differences in downstream signaling between the different designed ligands to differences in the patterns of induced receptor autophosphorylation: the full agonist, like insulin, induces autophosphorylation at tyrosine 960, which is recognized by the effector SHC, while the antagonist and biased agonist do not. As a consequence, SHC is not phosphorylated as efficiently by the activated IR for the biased agonist-and not at all for the antagonist; as SHC, in turn, activates the MAPK pathway, the partial agonist activates this pathway much less than the full agonist and native insulin. The differences in receptor phosphorylation and MAPK pathway activation are likely also responsible for the differences we observe in the rates of agonist-induced endocytosis (Figure 4). Finally, the reduction in MAPK pathway activation is likely responsible for the reduction we observe in ability to control glucose levels in vivo by the biased agonist.

The ability to fine-tune signaling through a key cell-surface receptor by generating a series of full and partial/biased agonists provides a powerful new approach for probing signaling biochemistry and biology, as well as for developing new compounds with potential therapeutic activity. The potency, signaling diversity, and IR selectivity of these synthetic agonists open exciting therapeutic opportunities. Our AKT-selective partial agonists may be particularly valuable for diabetes management in patients with cancer, given the potential cancer-inducing properties of insulin. 70-73 Unlike insulin, both partial and full agonists did not promote cancer cell proliferation while maintaining metabolic activity in normal cells, likely due to their strict IR selectivity and lack of IGF1R activation. This property could be advantageous in a range of diseases where off-target IGF1R signaling is problematic, including cancer, autoimmune disorders, and thyroid eye disease. 74-76 Finally, the ability of these agonists to bind and activate insulin-binding-deficient or diseasecausing IR mutants highlights their potential in treating rare but devastating conditions that currently lead to early morbidity. Together, these molecules represent a powerful toolkit for dissecting IR signaling mechanisms and a starting point for developing next-generation therapies.

Limitations of the study

We do not fully understand the origins of the differences in receptor autophosphorylation induced by the designed agonists: the conformation of the receptors in our cryo-EM structures of the receptor-agonist complexes are similar to each other (and to that induced by native insulin). A clue may be the lower resolution of the biased agonist structure, which may indicate greater conformational dynamics, resulting in the less effective autophosphorylation we observe at sites required for recruiting the MAPK effector SHC. For potential therapeutic applications, the in vivo metabolic effects of our biased agonists are not fully characterized, and the relatively large size of these agonists compared with insulin may limit penetration into muscle and adipose but favor liver delivery, explaining the sustained glucose-lowering effects yet potential hypoglycemia risk. Future live-cell, structural, and pharmacokinetic studies will be essential for fully characterizing the signaling mechanism and potential therapeutic utility of our new class of synthetic insulin agonists.

RESOURCE AVAILABILITY

Lead contact

Further information and requests for resources and reagents should be directed to the lead contact, Eunhee Choi (ec3477@cumc.columbia.edu).

Materials availability

Reagents described in this paper are available from the lead contact with a completed materials transfer agreement.

Data and code availability

- Source data were deposited at the following link: (https://data.mendeley.com/preview/d79cyzwtcy?a=f598ae87-b17c-408d-8b36-881480cb388a). The models and cryo-EM maps generated in this study were deposited at the PDB and EMDB under codes PDB: 9DNN, EMD-47043 (insulin/S2B/mouse IR complex); PDB: 9DN6, EMD-47031 (RF-405/human IR complex); and PDB: 9DNI, EMD-47041 (S2-F1-S1/human IR complex), and all data are publicly available as of the date of publication.
- This paper does not report original code.
- Any additional information required to reanalyze the data reported in this
 paper is available from the lead contact upon request.

ACKNOWLEDGMENTS

This work is supported in part by grants from the National Institutes of Health (R35GM142937 and R01DK132361 to E.C. and R35GM156386 to X.-c.B.), the Howard Hughes Medical Institute (D.B.), the Audacious Project (to D.L.,

⁽C) ITT in high-fat-diet-fed mice. Mean \pm SEM; Humulin, n = 8; S2-F1-S1 and RF-409, n = 7. Significance by two-way ANOVA vs. Humulin; *p < 0.05, ***p < 0.01, ****p < 0.001, ****p < 0.0001.

⁽D) ITT in high-fat-diet-fed mice. Mean \pm SEM. Humulin, n = 8; S2-F1-S1 and RF-409, n = 7. Significance by two-way ANOVA vs. Humulin; *p < 0.05, ***p < 0.01, ****p < 0.001, ****p < 0.0001.

⁽E) Efficacy (Emax relative to insulin-activated IR WT) and property of IR agonists. Mean \pm SD. Significance by one-way ANOVA vs. insulin; *p < 0.05, **p < 0.01, ***p < 0.001, ****p < 0.0001. Bar represents fold changes relative to insulin; values exceeding insulin are shown at the same bar height as insulin maximum values. N.D., not determined.

⁽F) Proposed model: rigidly linked agonists (RF-405 and RF-409) stabilize full IR activation, flexibly linked agonists (S2-F1-S1 and S2-F5-S1) yield partial activation, and S1-Fn-S2 constructs act as antagonists by competing with insulin.

Article



P.V., and X.W.), Open Philanthropy Project Improving Protein Design Fund (to B.C. and S.G.), the Irma T. Hirschl award (to E.C.), the Feldstein Medical Foundation (to E.C.), and the Welch Foundation (I-1944 to X.-c.B.). Cryo-EM data were collected at the UT Southwestern Medical Center Cryo-Electron Microscopy Facility, funded in part by the Cancer Prevention and Research Institute of Texas Core Facility (RP170644). We thank Dr. Stoddard for Cryo-EM facility access and Drs. Ronald Kahn and Hirofumi Nagao for sharing IR/IGF1R DKO preadipocytes. This research used resources of the NIH funding to the Columbia Center for Translational Immunology Flow Cytometry Core and Columbia Diabetes Center (P30DK063608) and Columbia Digestive and Liver Diseases Research Center (1P30DK132710). X.-c.B. is a Virginia Murchison Linthicum Scholar in Medical Research at UTSW. Graphical abstract created in BioRender. Choi, E. (2025) https://BioRender.com/s9mm6ad.

AUTHOR CONTRIBUTIONS

X.W., E.C., X.-c.B., and D.B. designed the research. X.W. and P.V. designed and characterized the biochemical properties of designed binders. S.C., M. N., C.H., M.G., Y.-C.L., and E.C. screened and characterized the designed binders in cultured cells and analyzed cellular assays. A.H., S.C., M.H., D. A., and E.C. characterized the designed binders in mice and analyzed animal experiments. K.C., J.L., W.A., and X.-c.B. prepared samples, collected data, and built the cryo-EM models. X.W., E.C., X.-c.B., and D.B. wrote the initial manuscript. All authors contributed to editing and discussing the manuscript.

DECLARATION OF INTERESTS

X.W., P.V., K.C., S.C., E.C., X.-c.B., and D.B. are co-inventors on a provisional patent (IP:50206.01US1) filed by the University of Washington, covering molecules and their uses described in this manuscript.

STAR*METHODS

Detailed methods are provided in the online version of this paper and include the following:

- KEY RESOURCES TABLE
- EXPERIMENTAL MODEL AND STUDY PARTICIPANT DETAILS
 - o Mouse strains and Husbandry
 - o Cell lines
- METHOD DETAILS
 - $\circ\,$ Computational design of the IR site-2 binders
 - $\circ\,$ Computational design of the linked binders
 - Yeast surface display screening for IR site 2 binders with FACS
 - o Protein binder expression and purification
 - o Biolayer interferometry (BLI)
 - Circular Dichroism Spectroscopy
 - o Protein expression and purification for cryo-EM
 - Cryo-EM data collection and image processing
 - Model building and refinement
 - Transfection and viral infection
 - IR signaling assay
 - $_{\odot}\,$ IR signaling analysis in vivo
 - Primary mouse hepatocytes isolation
 - Cell surface biotinylation and streptavidin pulldown
 - o Insulin tolerance test
 - Cell proliferation assay
- QUANTIFICATION AND STATISTICAL ANALYSIS

SUPPLEMENTAL INFORMATION

Supplemental information can be found online at https://doi.org/10.1016/j.molcel.2025.09.020.

Received: October 8, 2024 Revised: July 24, 2025 Accepted: September 18, 2025

REFERENCES

- Haeusler, R.A., McGraw, T.E., and Accili, D. (2018). Biochemical and cellular properties of insulin receptor signalling. Nat. Rev. Mol. Cell Biol. 19, 31–44. https://doi.org/10.1038/nrm.2017.89.
- Petersen, M.C., and Shulman, G.I. (2018). Mechanisms of Insulin Action and Insulin Resistance. Physiol. Rev. 98, 2133–2223. https://doi.org/10. 1152/physrev.00063.2017.
- White, M.F., and Kahn, C.R. (2021). Insulin action at a molecular level 100 years of progress. Mol. Metab. 52, 101304. https://doi.org/10.1016/j.molmet.2021.101304.
- Choi, E., Duan, C., and Bai, X.C. (2025). Regulation and function of insulin and insulin-like growth factor receptor signalling. Nat. Rev. Mol. Cell Biol. 26, 558–580. https://doi.org/10.1038/s41580-025-00826-3.
- Kasuga, M., Karlsson, F.A., and Kahn, C.R. (1982). Insulin stimulates the phosphorylation of the 95,000-dalton subunit of its own receptor. Science 215, 185–187. https://doi.org/10.1126/science.7031900.
- Kasuga, M., Zick, Y., Blithe, D.L., Crettaz, M., and Kahn, C.R. (1982). Insulin stimulates tyrosine phosphorylation of the insulin receptor in a cell-free system. Nature 298, 667–669. https://doi.org/10.1038/298667a0.
- 7. White, M.F., Maron, R., and Kahn, C.R. (1985). Insulin rapidly stimulates tyrosine phosphorylation of a Mr-185,000 protein in intact cells. Nature *318*, 183–186. https://doi.org/10.1038/318183a0.
- Sun, X.J., Rothenberg, P., Kahn, C.R., Backer, J.M., Araki, E., Wilden, P. A., Cahill, D.A., Goldstein, B.J., and White, M.F. (1991). Structure of the insulin receptor substrate IRS-1 defines a unique signal transduction protein. Nature 352, 73–77. https://doi.org/10.1038/352073a0.
- Freed, D.M., Bessman, N.J., Kiyatkin, A., Salazar-Cavazos, E., Byrne, P. O., Moore, J.O., Valley, C.C., Ferguson, K.M., Leahy, D.J., Lidke, D.S., et al. (2017). EGFR Ligands Differentially Stabilize Receptor Dimers to Specify Signaling Kinetics. Cell 171, 683–695.e18. https://doi.org/10. 1016/j.cell.2017.09.017.
- Lemmon, M.A., and Schlessinger, J. (2010). Cell signaling by receptor tyrosine kinases. Cell 141, 1117–1134. https://doi.org/10.1016/j.cell. 2010.06.011.
- Liu, H., Chen, X., Focia, P.J., and He, X. (2007). Structural basis for stem cell factor-KIT signaling and activation of class III receptor tyrosine kinases. EMBO J. 26, 891–901. https://doi.org/10.1038/sj.emboj.7601545.
- Leppänen, V.M., Prota, A.E., Jeltsch, M., Anisimov, A., Kalkkinen, N., Strandin, T., Lankinen, H., Goldman, A., Ballmer-Hofer, K., and Alitalo, K. (2010). Structural determinants of growth factor binding and specificity by VEGF receptor 2. Proc. Natl. Acad. Sci. USA 107, 2425–2430. https:// doi.org/10.1073/pnas.0914318107.
- Wiesmann, C., Fuh, G., Christinger, H.W., Eigenbrot, C., Wells, J.A., and de Vos, A.M. (1997). Crystal structure at 1.7 A resolution of VEGF in complex with domain 2 of the Fit-1 receptor. Cell 91, 695–704. https://doi.org/ 10.1016/s0092-8674(00)80456-0.
- Wiesmann, C., Ultsch, M.H., Bass, S.H., and de Vos, A.M. (1999). Crystal structure of nerve growth factor in complex with the ligand-binding domain of the TrkA receptor. Nature 401, 184–188. https://doi.org/10.1038/43705.
- Trenker, R., and Jura, N. (2020). Receptor tyrosine kinase activation: From the ligand perspective. Curr. Opin. Cell Biol. 63, 174–185. https://doi.org/ 10.1016/j.ceb.2020.01.016.
- Ullrich, A., Bell, J.R., Chen, E.Y., Herrera, R., Petruzzelli, L.M., Dull, T.J., Gray, A., Coussens, L., Liao, Y.C., and Tsubokawa, M. (1985). Human insulin receptor and its relationship to the tyrosine kinase family of oncogenes. Nature 313, 756–761. https://doi.org/10.1038/313756a0.



- Ebina, Y., Ellis, L., Jarnagin, K., Edery, M., Graf, L., Clauser, E., Ou, J.H., Masiarz, F., Kan, Y.W., and Goldfine, I.D. (1985). The human insulin receptor cDNA: the structural basis for hormone-activated transmembrane signalling. Cell 40, 747–758. https://doi.org/10.1016/0092-8674(85)90334-4.
- Uchikawa, E., Choi, E., Shang, G., Yu, H., and Bai, X.C. (2019). Activation mechanism of the insulin receptor revealed by cryo-EM structure of the fully liganded receptor-ligand complex. eLife 8, e48630. https://doi.org/ 10.7554/eLife.48630.
- An, W., Hall, C., Li, J., Hung, A., Wu, J., Park, J., Wang, L., Bai, X.C., and Choi, E. (2024). Activation of the insulin receptor by insulin-like growth factor 2. Nat. Commun. 15, 2609. https://doi.org/10.1038/s41467-024-46990-6.
- Li, J., Park, J., Mayer, J.P., Webb, K.J., Uchikawa, E., Wu, J., Liu, S., Zhang, X., Stowell, M.H.B., Choi, E., et al. (2022). Synergistic activation of the insulin receptor via two distinct sites. Nat. Struct. Mol. Biol. 29, 357–368. https://doi.org/10.1038/s41594-022-00750-6.
- Choi, E., and Bai, X.C. (2023). The Activation Mechanism of the Insulin Receptor: A Structural Perspective. Annu. Rev. Biochem. 92, 247–272. https://doi.org/10.1146/annurev-biochem-052521-033250.
- McKern, N.M., Lawrence, M.C., Streltsov, V.A., Lou, M.Z., Adams, T.E., Lovrecz, G.O., Elleman, T.C., Richards, K.M., Bentley, J.D., Pilling, P.A., et al. (2006). Structure of the insulin receptor ectodomain reveals a folded-over conformation. Nature 443, 218–221. https://doi.org/10.1038/ nature05106.
- Croll, T.I., Smith, B.J., Margetts, M.B., Whittaker, J., Weiss, M.A., Ward, C. W., and Lawrence, M.C. (2016). Higher-Resolution Structure of the Human Insulin Receptor Ectodomain: Multi-Modal Inclusion of the Insert Domain. Structure 24, 469–476. https://doi.org/10.1016/j.str.2015.12.014.
- Scapin, G., Dandey, V.P., Zhang, Z., Prosise, W., Hruza, A., Kelly, T., Mayhood, T., Strickland, C., Potter, C.S., and Carragher, B. (2018). Structure of the insulin receptor-insulin complex by single-particle cryo-EM analysis. Nature 556, 122–125. https://doi.org/10.1038/nature26153.
- Gutmann, T., Schäfer, I.B., Poojari, C., Brankatschk, B., Vattulainen, I., Strauss, M., and Coskun, Ü. (2020). Cryo-EM structure of the complete and ligand-saturated insulin receptor ectodomain. J. Cell Biol. 219, e201907210. https://doi.org/10.1083/jcb.201907210.
- Cao, L., Coventry, B., Goreshnik, I., Huang, B., Sheffler, W., Park, J.S., Jude, K.M., Marković, I., Kadam, R.U., Verschueren, K.H.G., et al. (2022). Design of protein-binding proteins from the target structure alone. Nature 605, 551–560. https://doi.org/10.1038/s41586-022-04654-9.
- Vázquez Torres, S., Leung, P.J.Y., Venkatesh, P., Lutz, I.D., Hink, F., Huynh, H.H., Becker, J., Yeh, A.H.W., Juergens, D., Bennett, N.R., et al. (2024). De novo design of high-affinity binders of bioactive helical peptides. Nature 626, 435–442. https://doi.org/10.1038/s41586-023-06953-1.
- Watson, J.L., Juergens, D., Bennett, N.R., Trippe, B.L., Yim, J., Eisenach, H.E., Ahern, W., Borst, A.J., Ragotte, R.J., Milles, L.F., et al. (2023). De novo design of protein structure and function with RFdiffusion. Nature 620, 1089–1100. https://doi.org/10.1038/s41586-023-06415-8.
- Zambaldi, V., La, D., Chu, A.E., Patani, H., Danson, A.E., Kwan, T.O.C., Frerix, T., Schneider, R.G., Saxton, D., Thillaisundaram, A., et al. (2024).
 De Novo Design of High-Affinity Protein Binders with AlphaProteo. Preprint at arXiv. https://doi.org/10.48550/arXiv.2409.08022.
- Moraga, I., Wernig, G., Wilmes, S., Gryshkova, V., Richter, C.P., Hong, W. J., Sinha, R., Guo, F., Fabionar, H., Wehrman, T.S., et al. (2015). Tuning cytokine receptor signaling by re-orienting dimer geometry with surrogate ligands. Cell 160, 1196–1208. https://doi.org/10.1016/j.cell.2015.02.011.
- Tsutsumi, N., Masoumi, Z., James, S.C., Tucker, J.A., Winkelmann, H., Grey, W., Picton, L.K., Moss, L., Wilson, S.C., Caveney, N.A., et al. (2023). Structure of the thrombopoietin-MPL receptor complex is a blueprint for biasing hematopoiesis. Cell 186, 4189–4203.e22. https://doi. org/10.1016/j.cell.2023.07.037.

- Sims, E.K., Carr, A.L.J., Oram, R.A., DiMeglio, L.A., and Evans-Molina, C. (2021). 100 years of insulin: celebrating the past, present and future of diabetes therapy. Nat. Med. 27, 1154–1164. https://doi.org/10.1038/s41591-021-01418-2.
- Hiranuma, N., Park, H., Baek, M., Anishchenko, I., Dauparas, J., and Baker, D. (2021). Improved protein structure refinement guided by deep learning based accuracy estimation. Nat. Commun. 12, 1340. https:// doi.org/10.1038/s41467-021-21511-x.
- Seino, S., and Bell, G.I. (1989). Alternative splicing of human insulin receptor messenger RNA. Biochem. Biophys. Res. Commun. 159, 312–316. https://doi.org/10.1016/0006-291x(89)92439-x.
- Park, J., Li, J., Mayer, J.P., Ball, K.A., Wu, J., Hall, C., Accili, D., Stowell, M. H.B., Bai, X.C., and Choi, E. (2022). Activation of the insulin receptor by an insulin mimetic peptide. Nat. Commun. 13, 5594. https://doi.org/10.1038/ s41467-022-33274-0.
- Bennett, N.R., Coventry, B., Goreshnik, I., Huang, B., Allen, A., Vafeados, D., Peng, Y.P., Dauparas, J., Baek, M., Stewart, L., et al. (2023). Improving de novo protein binder design with deep learning. Nat. Commun. 14, 2625. https://doi.org/10.1038/s41467-023-38328-5.
- Li, J., Choi, E., Yu, H., and Bai, X.C. (2019). Structural basis of the activation of type 1 insulin-like growth factor receptor. Nat. Commun. 10, 4567. https://doi.org/10.1038/s41467-019-12564-0.
- Kavran, J.M., McCabe, J.M., Byrne, P.O., Connacher, M.K., Wang, Z., Ramek, A., Sarabipour, S., Shan, Y., Shaw, D.E., Hristova, K., et al. (2014). How IGF-1 activates its receptor. eLife 3, e03772. https://doi. org/10.7554/eLife.03772.
- Kjeldsen, T., Andersen, A.S., Wiberg, F.C., Rasmussen, J.S., Schäffer, L., Balschmidt, P., Møller, K.B., and Møller, N.P. (1991). The ligand specificities of the insulin receptor and the insulin-like growth factor I receptor reside in different regions of a common binding site. Proc. Natl. Acad. Sci. USA 88, 4404–4408. https://doi.org/10.1073/pnas.88.10.4404.
- Schumacher, R., Mosthaf, L., Schlessinger, J., Brandenburg, D., and Ullrich, A. (1991). Insulin and insulin-like growth factor-1 binding specificity is determined by distinct regions of their cognate receptors. J. Biol. Chem. 266, 19288–19295. https://doi.org/10.1016/S0021-9258(18)54996-6.
- Jensen, M., Hansen, B., De Meyts, P., Schäffer, L., and Ursø, B. (2007).
 Activation of the insulin receptor by insulin and a synthetic peptide leads to divergent metabolic and mitogenic signaling and responses. J. Biol. Chem. 282, 35179–35186. https://doi.org/10.1074/jbc.M704599200.
- Kanter, J.E., Kramer, F., Barnhart, S., Duggan, J.M., Shimizu-Albergine, M., Kothari, V., Chait, A., Bouman, S.D., Hamerman, J.A., Hansen, B.F., et al. (2018). A Novel Strategy to Prevent Advanced Atherosclerosis and Lower Blood Glucose in a Mouse Model of Metabolic Syndrome. Diabetes 67, 946–959. https://doi.org/10.2337/db17-0744.
- Liao, Z., Zhang, C., Ding, L., Moyers, J.S., Tang, J.X., and Beals, J.M. (2022). Comprehensive insulin receptor phosphorylation dynamics profiled by mass spectrometry. FEBS J. 289, 2657–2671. https://doi.org/10.1111/febs.16299.
- Eck, M.J., Dhe-Paganon, S., Trüb, T., Nolte, R.T., and Shoelson, S.E. (1996). Structure of the IRS-1 PTB domain bound to the juxtamembrane region of the insulin receptor. Cell 85, 695–705. https://doi.org/10.1016/s0092-8674(00)81236-2
- He, W., O'Neill, T.J., and Gustafson, T.A. (1995). Distinct modes of interaction of SHC and insulin receptor substrate-1 with the insulin receptor NPEY region via non-SH2 domains. J. Biol. Chem. 270, 23258–23262. https://doi.org/10.1074/jbc.270.40.23258.
- Cai, W., Sakaguchi, M., Kleinridders, A., Gonzalez-Del Pino, G., Dreyfuss, J.M., O'Neill, B.T., Ramirez, A.K., Pan, H., Winnay, J.N., Boucher, J., et al. (2017). Domain-dependent effects of insulin and IGF-1 receptors on signalling and gene expression. Nat. Commun. 8, 14892. https://doi.org/10. 1038/ncomms14892.
- 47. Paz, K., Voliovitch, H., Hadari, Y.R., Roberts, C.T., Jr., LeRoith, D., and Zick, Y. (1996). Interaction between the insulin receptor and its

Article



- downstream effectors. Use of individually expressed receptor domains for structure/function analysis. J. Biol. Chem. 271, 6998–7003. https://doi.org/10.1074/jbc.271.12.6998.
- Gehart, H., Kumpf, S., Ittner, A., and Ricci, R. (2010). MAPK signalling in cellular metabolism: stress or wellness? EMBO Rep. 11, 834–840. https://doi.org/10.1038/embor.2010.160.
- Hall, C., Yu, H., and Choi, E. (2020). Insulin receptor endocytosis in the pathophysiology of insulin resistance. Exp. Mol. Med. 52, 911–920. https://doi.org/10.1038/s12276-020-0456-3.
- Chen, Y., Huang, L., Qi, X., and Chen, C. (2019). Insulin Receptor Trafficking: Consequences for Insulin Sensitivity and Diabetes. Int. J. Mol. Sci. 20, 5007. https://doi.org/10.3390/ijms20205007.
- Choi, E., Kikuchi, S., Gao, H., Brodzik, K., Nassour, I., Yopp, A., Singal, A. G., Zhu, H., and Yu, H. (2019). Mitotic regulators and the SHP2-MAPK pathway promote IR endocytosis and feedback regulation of insulin signaling. Nat. Commun. 10, 1473. https://doi.org/10.1038/s41467-019-09318-3.
- Semple, R.K., Savage, D.B., Cochran, E.K., Gorden, P., and O'rahilly, S. (2011). Genetic syndromes of severe insulin resistance. Endocr. Rev. 32, 498–514. https://doi.org/10.1210/er.2010-0020.
- Melvin, A., O'rahilly, S., and Savage, D.B. (2018). Genetic syndromes of severe insulin resistance. Curr. Opin. Genet. Dev. 50, 60–67. https://doi. org/10.1016/j.gde.2018.02.002.
- Musso, C., Cochran, E., Moran, S.A., Skarulis, M.C., Oral, E.A., Taylor, S., and Gorden, P. (2004). Clinical course of genetic diseases of the insulin receptor (type A and Rabson-Mendenhall syndromes): a 30-year prospective. Med. Baltim. 83, 209–222. https://doi.org/10.1097/01.md.0000133 625.73570.54.
- Grasso, V., Colombo, C., Favalli, V., Galderisi, A., Rabbone, I., Gombos, S., Bonora, E., Massa, O., Meschi, F., Cerutti, F., et al. (2013). Six cases with severe insulin resistance (SIR) associated with mutations of insulin receptor: Is a Bartter-like syndrome a feature of congenital SIR? Acta Diabetol. 50, 951–957. https://doi.org/10.1007/s00592-013-0490-x.
- Kadowaki, T., Kadowaki, H., Rechler, M.M., Serrano-Rios, M., Roth, J., Gorden, P., and Taylor, S.I. (1990). Five mutant alleles of the insulin receptor gene in patients with genetic forms of insulin resistance. J. Clin. Invest. 86, 254–264. https://doi.org/10.1172/JCI114693.
- Bamborschke, D., Özdemir, Ö., Kreutzer, M., Motameny, S., Thiele, H., Kribs, A., Dötsch, J., Altmüller, J., Nürnberg, P., and Cirak, S. (2021). Ultra-rapid emergency genomic diagnosis of Donahue syndrome in a preterm infant within 17 hours. Am. J. Med. Genet. A 185, 90–96. https://doi.org/10.1002/ajmg.a.61917.
- 58. Hart, L.M., Lindhout, D., Van der Zon, G.C., Kayserilli, H., Apak, M.Y., Kleijer, W.J., Van der Vorm, E.R., and Maassen, J.A. (1996). An insulin receptor mutant (Asp707 -> Ala), involved in leprechaunism, is processed and transported to the cell surface but unable to bind insulin. J. Biol. Chem. 271, 18719–18724. https://doi.org/10.1074/jbc.271.31.18719.
- Shahid, R.K., Ahmed, S., Le, D., and Yadav, S. (2021). Diabetes and Cancer: Risk, Challenges, Management and Outcomes. Cancers 13, 5735. https://doi.org/10.3390/cancers13225735.
- Zhang, A.M.Y., Xia, Y.H., Lin, J.S.H., Chu, K.H., Wang, W.C.K., Ruiter, T.J. J., Yang, J.C.C., Chen, N., Chhuor, J., Patil, S., et al. (2023). Hyperinsulinemia acts via acinar insulin receptors to initiate pancreatic cancer by increasing digestive enzyme production and inflammation. Cell Metab. 35, 2119–2135.e5. https://doi.org/10.1016/j.cmet.2023. 10.003.
- Rogava, M., Aprati, T.J., Chi, W.-Y., Melms, J.C., Hug, C., Davis, S.H., Earlie, E.M., Chung, C., Deshmukh, S.K., Wu, S., et al. (2024). Loss of Pip4k2c confers liver-metastatic organotropism through insulin-dependent PI3K-AKT pathway activation. Nat. Cancer 5, 433–447. https://doi. org/10.1038/s43018-023-00704-x.
- Rey-Reñones, C., Baena-Díez, J.M., Aguilar-Palacio, I., Miquel, C., and Grau, M. (2021). Type 2 Diabetes Mellitus and Cancer: Epidemiology,

- Physiopathology and Prevention. Biomedicines 9, 1429. https://doi.org/10.3390/biomedicines9101429.
- Belfiore, A., Frasca, F., Pandini, G., Sciacca, L., and Vigneri, R. (2009). Insulin receptor isoforms and insulin receptor/insulin-like growth factor receptor hybrids in physiology and disease. Endocr. Rev. 30, 586–623. https://doi.org/10.1210/er.2008-0047.
- 64. Pearson-Stuttard, J., Papadimitriou, N., Markozannes, G., Cividini, S., Kakourou, A., Gill, D., Rizos, E.C., Monori, G., Ward, H.A., Kyrgiou, M., et al. (2021). Type 2 Diabetes and Cancer: An Umbrella Review of Observational and Mendelian Randomization Studies. Cancer Epidemiol. Biomarkers Prev. 30, 1218–1228. https://doi.org/10.1158/1055-9965.EPI-20-1245.
- 65. Rocchi, S., Tartare-Deckert, S., Sawka-Verhelle, D., Gamha, A., and van Obberghen, E. (1996). Interaction of SH2-containing protein tyrosine phosphatase 2 with the insulin receptor and the insulin-like growth factor-I receptor: studies of the domains involved using the yeast two-hybrid system. Endocrinology 137, 4944–4952. https://doi.org/10.1210/endo.137.11.8895367.
- Myers, M.G., Jr., Mendez, R., Shi, P., Pierce, J.H., Rhoads, R., and White, M.F. (1998). The COOH-terminal tyrosine phosphorylation sites on IRS-1 bind SHP-2 and negatively regulate insulin signaling. J. Biol. Chem. 273, 26908–26914. https://doi.org/10.1074/jbc.273.41.26908.
- 67. Chen, Y.N.P., LaMarche, M.J., Chan, H.M., Fekkes, P., Garcia-Fortanet, J., Acker, M.G., Antonakos, B., Chen, C.H.T., Chen, Z., Cooke, V.G., et al. (2016). Allosteric inhibition of SHP2 phosphatase inhibits cancers driven by receptor tyrosine kinases. Nature 535, 148–152. https://doi.org/10.1038/nature18621.
- Hof, P., Pluskey, S., Dhe-Paganon, S., Eck, M.J., and Shoelson, S.E. (1998). Crystal structure of the tyrosine phosphatase SHP-2. Cell 92, 441–450. https://doi.org/10.1016/s0092-8674(00)80938-1.
- Nichols, R.J., Haderk, F., Stahlhut, C., Schulze, C.J., Hemmati, G., Wildes, D., Tzitzilonis, C., Mordec, K., Marquez, A., Romero, J., et al. (2018). RAS nucleotide cycling underlies the SHP2 phosphatase dependence of mutant BRAF-, NF1- and RAS-driven cancers. Nat. Cell Biol. 20, 1064– 1073. https://doi.org/10.1038/s41556-018-0169-1.
- Ling, S., Zaccardi, F., Issa, E., Davies, M.J., Khunti, K., and Brown, K. (2023). Inequalities in cancer mortality trends in people with type 2 diabetes: 20 year population-based study in England. Diabetologia 66, 657–673. https://doi.org/10.1007/s00125-022-05854-8.
- Pearson-Stuttard, J., Bennett, J., Cheng, Y.J., Vamos, E.P., Cross, A.J., Ezzati, M., and Gregg, E.W. (2021). Trends in predominant causes of death in individuals with and without diabetes in England from 2001 to 2018: an epidemiological analysis of linked primary care records. Lancet Diabetes Endocrinol. 9, 165–173. https://doi.org/10.1016/S2213-8587(20)30431-9.
- Song, M. (2021). Cancer overtakes vascular disease as leading cause of excess death associated with diabetes. Lancet Diabetes Endocrinol. 9, 131–133. https://doi.org/10.1016/S2213-8587(21)00016-4.
- Leitner, B.P., Siebel, S., Akingbesote, N.D., Zhang, X., and Perry, R.J. (2022). Insulin and cancer: a tangled web. Biochem. J. 479, 583–607. https://doi.org/10.1042/BCJ20210134.
- Smith, T.J., and Janssen, J.A.M.J.L. (2019). Insulin-like Growth Factor-I Receptor and Thyroid-Associated Ophthalmopathy. Endocr. Rev. 40, 236–267. https://doi.org/10.1210/er.2018-00066.
- Tsui, S., Naik, V., Hoa, N., Hwang, C.J., Afifiyan, N.F., Sinha Hikim, A., Gianoukakis, A.G., Douglas, R.S., and Smith, T.J. (2008). Evidence for an association between thyroid-stimulating hormone and insulin-like growth factor 1 receptors: a tale of two antigens implicated in Graves' disease. J. Immunol. 181, 4397–4405. https://doi.org/10.4049/jimmunol.181. 6.4397.
- Buck, E., Gokhale, P.C., Koujak, S., Brown, E., Eyzaguirre, A., Tao, N., Rosenfeld-Franklin, M., Lerner, L., Chiu, M.I., Wild, R., et al. (2010). Compensatory insulin receptor (IR) activation on inhibition of insulin-like growth factor-1 receptor (IGF-1R): rationale for cotargeting IGF-1R and



Molecular Cell Article

- IR in cancer. Mol. Cancer Ther. 9, 2652–2664. https://doi.org/10.1158/1535-7163.MCT-10-0318.
- Choi, E., Zhang, X., Xing, C., and Yu, H. (2016). Mitotic Checkpoint Regulators Control Insulin Signaling and Metabolic Homeostasis. Cell 166, 567–581. https://doi.org/10.1016/j.cell.2016.05.074.
- Sanjana, N.E., Shalem, O., and Zhang, F. (2014). Improved vectors and genome-wide libraries for CRISPR screening. Nat. Methods 11, 783–784. https://doi.org/10.1038/nmeth.3047.
- Morales-Perez, C.L., Noviello, C.M., and Hibbs, R.E. (2016). Manipulation of Subunit Stoichiometry in Heteromeric Membrane Proteins. Structure 24, 797–805. https://doi.org/10.1016/j.str.2016.03.004.
- Duhovny, D., Nussinov, R., and Wolfson, H.J. (2002). Efficient Unbound Docking of Rigid Molecules. In Algorithms in Bioinformatics Lecture Notes in Computer Science, R. Guigó and D. Gusfield, eds. (Springer Berlin Heidelberg), pp. 185–200. https://doi.org/10.1007/3-540-45784-4_14.
- Leman, J.K., Weitzner, B.D., Lewis, S.M., Adolf-Bryfogle, J., Alam, N., Alford, R.F., Aprahamian, M., Baker, D., Barlow, K.A., Barth, P., et al. (2020). Macromolecular modeling and design in Rosetta: recent methods and frameworks. Nat. Methods 17, 665–680. https://doi.org/10.1038/ s41592-020-0848-2.
- Dauparas, J., Anishchenko, I., Bennett, N., Bai, H., Ragotte, R.J., Milles, L. F., Wicky, B.I.M., Courbet, A., de Haas, R.J., Bethel, N., et al. (2022). Robust deep learning-based protein sequence design using ProteinMPNN. Science 378, 49–56. https://doi.org/10.1126/science.add2187.
- Jumper, J., Evans, R., Pritzel, A., Green, T., Figurnov, M., Ronneberger, O., Tunyasuvunakool, K., Bates, R., Žídek, A., Potapenko, A., et al. (2021). Highly accurate protein structure prediction with AlphaFold. Nature 596, 583–589. https://doi.org/10.1038/s41586-021-03819-2.
- Zheng, S.Q., Palovcak, E., Armache, J.P., Verba, K.A., Cheng, Y., and Agard, D.A. (2017). MotionCor2: anisotropic correction of beam-induced motion for improved cryo-electron microscopy. Nat. Methods 14, 331–332. https://doi.org/10.1038/nmeth.4193.
- Zivanov, J., Otón, J., Ke, Z., Von Kügelgen, A., Pyle, E., Qu, K., Morado, D., Castaño-Díez, D., Zanetti, G., Bharat, T.A.M., et al. (2022). A Bayesian approach to single-particle electron cryo-tomography in RELION-4.0. eLife 11, e83724. https://doi.org/10.7554/eLife.83724.
- Emsley, P., Lohkamp, B., Scott, W.G., and Cowtan, K. (2010). Features and development of Coot. Acta Crystallogr. D Biol. Crystallogr. 66, 486–501. https://doi.org/10.1107/S0907444910007493.
- Adams, P.D., Afonine, P.V., Bunkóczi, G., Chen, V.B., Davis, I.W., Echols, N., Headd, J.J., Hung, L.-W., Kapral, G.J., Grosse-Kunstleve, R.W., et al. (2010). PHENIX: a comprehensive Python-based system for macromolec-

- ular structure solution. Acta Crystallogr. D 66, 213–221. https://doi.org/10. 1107/S0907444909052925.
- Pettersen, E.F., Goddard, T.D., Huang, C.C., Meng, E.C., Couch, G.S., Croll, T.I., Morris, J.H., and Ferrin, T.E. (2021). UCSF ChimeraX: Structure visualization for researchers, educators, and developers. Protein Sci. 30, 70–82. https://doi.org/10.1002/pro.3943.
- Nagao, H., Cai, W., Wewer Albrechtsen, N.J., Steger, M., Batista, T.M., Pan, H., Dreyfuss, J.M., Mann, M., and Kahn, C.R. (2021). Distinct signaling by insulin and IGF-1 receptors and their extra- and intracellular domains. Proc. Natl. Acad. Sci. USA 118, e2019474118. https://doi.org/ 10.1073/pnas.2019474118.
- Wicky, B.I.M., Milles, L.F., Courbet, A., Ragotte, R.J., Dauparas, J., Kinfu, E., Tipps, S., Kibler, R.D., Baek, M., DiMaio, F., et al. (2022). Hallucinating symmetric protein assemblies. Science 378, 56–61. https://doi.org/10. 1126/science.add1964.
- 91. Zhang, K. (2016). Gctf: Real-time CTF determination and correction.
 J. Struct. Biol. 193, 1–12. https://doi.org/10.1016/j.jsb.2015.11.003.
- Kimanius, D., Dong, L., Sharov, G., Nakane, T., and Scheres, S.H.W. (2021). New tools for automated cryo-EM single-particle analysis in RELION-4.0. Biochem. J. 478, 4169–4185. https://doi.org/10.1042/BCJ20210708.
- Liebschner, D., Afonine, P.V., Baker, M.L., Bunkóczi, G., Chen, V.B., Croll, T.I., Hintze, B., Hung, L.W., Jain, S., McCoy, A.J., et al. (2019). Macromolecular structure determination using X-rays, neutrons and electrons: recent developments in Phenix. Acta Crystallogr. D Struct. Biol. 75, 861–877. https://doi.org/10.1107/S2059798319011471.
- Chen, V.B., Arendall, W.B., 3rd, Headd, J.J., Keedy, D.A., Immormino, R. M., Kapral, G.J., Murray, L.W., Richardson, J.S., and Richardson, D.C. (2010). MolProbity: all-atom structure validation for macromolecular crystallography. Acta Crystallogr. D Biol. Crystallogr. 66, 12–21. https://doi.org/10.1107/S0907444909042073.
- Pettersen, E.F., Goddard, T.D., Huang, C.C., Couch, G.S., Greenblatt, D. M., Meng, E.C., and Ferrin, T.E. (2004). UCSF Chimera–a visualization system for exploratory research and analysis. J. Comput. Chem. 25, 1605–1612. https://doi.org/10.1002/jcc.20084
- Li, J., Wu, J., Hall, C., Bai, X.C., and Choi, E. (2022). Molecular basis for the role of disulfide-linked alphaCTs in the activation of insulin-like growth factor 1 receptor and insulin receptor. eLife 11, e81286. https://doi.org/10. 7554/eLife.81286.
- Ramachandran, K.V., and Margolis, S.S. (2017). A mammalian nervoussystem-specific plasma membrane proteasome complex that modulates neuronal function. Nat. Struct. Mol. Biol. 24, 419–430. https://doi.org/10. 1038/nsmb.3389.

Article



STAR*METHODS

KEY RESOURCES TABLE

REAGENT or RESOURCE	SOURCE	IDENTIFIER
Antibodies		
Anti-IR (CT-3)	Santa Cruz	Cat#sc-57342; RRID: AB_784102
Anti-IR-pY1150/1151	Cell signaling	Cat#3024; RRID: AB_331253
anti-IR-pY1146	Cell signaling	Cat#80732S; RRID:AB_2799958
anti-IR-Y1316	Invitrogen	Cat#44-807G; RRID: AB_2533764
anti-IR-Y1322	Invitrogen	Cat#44-809G; RRID: AB_2533765
anti-IR-pY960	Invitrogen	Cat#44-800G; RRID: AB_2533760
anti-pY239/240 SHC	Cell signaling	Cat#2434; RRID: AB_10841301
Anti-SHC PG-797	Santa Cruz	Cat#sc-967; RRID: AB_628249
Anti-pY608 IRS1	Millipore	Cat#09-432; RRID: AB_1163457
Anti-IRS1	BD Biosciences	Cat#611394; RRID: AB_398916
Anti-pS473 AKT D9E	Cell signaling	Cat#4060; RRID: AB_2315049
Anti-AKT 40D4	Cell signaling	Cat#2920; RRID: AB_1147620
Anti-pERK1/2 197G2	Cell signaling	Cat#4377; RRID: AB_331775
Anti-ERK1/2 L34F12	Cell signaling	Cat#4696; RRID: AB_390780
Anti-IGF1R beta Monoclonal Antibody (Zl001)	Invitrogen	Cat#39-6700; RRID: AB_2533429
Anti-myc	Roche	Cat#11667149001; RRID: AB_390912
Anti-rabbit immunoglobulin G (IgG) (H+L) Dylight 800 conjugates	Cell signaling	Cat#5151; RRID: AB_10697505
Anti-mouse IgG (H+L) Dylight 680 conjugates	Cell signaling	Cat#5470; RRID: AB_10696895
Anti-rabbit IgG (H+L) Dylight 680 conjugates	Cell signaling	Cat#5366S; RRID: AB_10693812
Anti-mouse IgG (H+L) Dylight 800 conjugates	Cell signaling	Cat#5257S; RRID: AB_10693543
Anti-beta catenin	Cell signaling	Cat#8480; RRID: AB_11127855
Anti-Actin	Santa Cruz	Cat#sc-47778; RRID: AB_626632
FITC anti-BrdU antibody	BD	Cat#556028; RRID: AB_396304
Anti-c-Myc fluorescein isothiocyanate (FITC)	Miltenyi Biotech	Cat#130-048-701; RRID: AB_244371
BrdU monoclonal antibody	Thermo Fisher Scientific	Cat#MA3-071; RRID: AB_10986341
Bacterial and virus strains		
E. coli, strain: Stbl3	Invitrogen	Cat#C737303
E.coli, strain: BL21 DE3	NEB	C2527I-81
E. coli, strain: DH10Bac	Thermo Fisher Scientific	Cat# 10361012
E. coli, strain: HST08	Takara Bio	Cat# 636763
Chemicals, peptides, and recombinant proteins	S	
Insulin	Sigma	Cat#I2526
Humulin	Eli Lilly	NDC 0002-8215-01
Polybrene	MedChemExpress	Cat#HY-112735
	<u></u>	0.1/44440000
Puromycin	Gibco	Cat#A1113803
Puromycin Blasticidin	Gibco Gibco	Cat#A1113803 Cat#R21001



Continued		
REAGENT or RESOURCE	SOURCE	IDENTIFIER
HEPES	Fisher Scientific	Cat#BP299-1
NaCl	Fisher Scientific	Cat#BP358-212
Glycerol	Acros organic	Cat#15892-0010
Triton X-100	Sigma	Cat#X-100
EDTA	Thermo Scientific	Cat#1861283
Sodium fluoride	Sigma	Cat#215309
Sodium orthovanadate	Sigma	Cat#S6508
Sodium pyrophosphate	Sigma	Cat#P8010
Dithiothreito	Thermo Scientific	Cat#R0861
Phenylmethylsulfonyl fluoride	Sigma	Cat#P7626
cOmplete Protease Inhibitor Cocktail	Roche	Cat#12352200
PhosSTOP	Roche	Cat#12352204
Γurbo nuclease	Accelagen	Cat#NC0298896
PBS	Corning	Cat#21-030-CM
PBS	Fisher Scientific	Cat#10010023
EZ linkTM Sulfo-NHS-LC-Biotin	Thermo Fisher	Cat#21335
RIPA buffer	Thermo Fisher	Cat#89901
Halt Protease & Phosphatase inhibitor	Thermo Fisher	Cat#78442
cocktail	memo i silei	Oddin 10442
streptavidin magnetic beads	Thermo Fisher	Cat#88817
Villiams' Medium E	Life Technologies	Cat#12551032
Dulbecco's modified Eagle's	Thermo Fisher	Cat#11965118
medium (DMEM)		
Fetal bovine serum	Gibco	Cat#A5256701
Penicillin/streptomycin	Fisher scientific	Cat#15140122
glutamine	Thermo Fisher	Cat#25030081
FreeStyleTM293 Expression Medium	Gibco	Cat# 12338018
SF900 II SFM	Gibco	Cat# 10902096
CTUG medium Complete supplement mixture -ura -trp	MP Biomedicals	114520512-CF
SGCAA medium	Teknova	Cat #2S0542
Autoinducing TBII media	In house	N/A
HBS-EP buffer	Cytiva Life Sciences	Cat#BR100669
Bovine Serum Albumin	SigmaAldrich	Cat#A8806
Streptavidin-phycoerythrin SAPE	ThermoFisher	Cat# S866
Bovine pancreas DNasel	Sigma-Aldrich	Cat#11284932001
Cellfectin	Gibco	Cat#10362100
Dodecyl maltoside (DDM)	Anatrace	Cat # D310S
midazol	Sigma	1370981000
NHS-Activated Sepharose	GE Healthcare	Cat#17-0906-01
Sodium butyrate	Sigma	Cat# 303410
CaCl ₂	Sigma	Cat# C4901
HRV-3C protease	Uchikawa et al. ¹⁸	N/A
100 kDa cutoff concentrator	Millipore	Cat#UFC5100
Collagen	Sigma	Cat#C3867
Dexamethasone	Sigma	Cat# D4902-25MG
Glycine	Fisher	Cat# BP381-1
•		
Hydrochloric acid	Fisher	Cat# RD2919 4
Absolute ethanol	Fisher	Cat# BP2818-4
Propidium iodide	BD	Cat#550825

Article



Continued		
REAGENT or RESOURCE	SOURCE	IDENTIFIER
IR extracellular domain (ECD)	ACROBIOsystems	INR-H82E6
IGF1R ECD	ACROBIOsystems	IGR-H82E3
Insulin ValA3E	Li et al. ²⁰	N/A
Insulin LeuA13R	Li et al. ²⁰	N/A
PicoLab® Rodent Diet 20	Lab diet	Cat#5053
Rodent Diet With 60 kcal% Fat	Research Diets	Cat# D12492
NEBuilder HiFi DNA Assembly Cloning kit	New England Biolabs	E5520S
Perfusion buffer	Gibco	17701-038
Digestion buffer	Gibco	17703-034
LB broth	Sigma	71753-M
Critical commercial assays		
Micro BCA Protein Assay Kit	Thermo Scientific	Cat#23235
CONTOUR NEXT Blood Glucose Test Strips for Diabetes	Contour Next	Cat#B07CF8C4VX
Contour next blood glucose monitoring	Contour Next	Cat#B0BWDX6Q1G
QIAprep Spin Miniprep Kit	Qiagen	Cat#27104
Deposited data		
Mendeley dataset	This paper	https://data.mendeley.com/preview/ d79cyzwtcy?a=f598ae87-b17c-408d- 8b36-881480cb388a
Cryo-EM map of Insulin/S2B/mouse IR complex	This paper	EMD-47043; PDB: 9DNN
Cryo-EM map of RF-405/human IR complex	This paper	EMD-47031; PDB: 9DN6
Cryo-EM map of S2-F1-S1/human IR complex	This paper	EMD-47041; PDB: 9DNI
Cryo-EM map of insulin/human IR complex	Uchikawa et al. ¹⁸	PDB:6PXV
Structure of human IR ectodomain	Croll et al. ²³	PDB: 4ZXB
Cryo-EM map of S597/mouse IR complex	Park et al. ³⁵	PDB: 8DTL
Experimental models: Cell lines		
C2C12	ATCC	CRL-1722
C2C12-IR	This paper	N/A
MCF7	ATCC	HTB-22
MCF7 IGF1R KO	This paper	N/A
DKO IR-B	Dr. Ronald Kahn	N/A
DKO IR-A	Dr. Ronald Kahn	N/A
FreeStyleTM293-F	Invitrogen	Cat#R79007
SF9	Invitrogen	Cat#11496015
293FT	Invitrogen	Cat#R70007
Experimental models: Organisms/strains		
Mice C57BL/6J	Jackson Laboratory	Strain #:000664; RRID:IMSR JAX:000664
S. cerevisiae, strain: EBY-100	ATCC	MYA-4941
Oligonucleotides		
gRNA mouse IGF1R:	This study	N/A
CACCGCTATGGTGGAGAGGTAACAG	This study	
gRNA human IGF1R: CACCGGAGAACGACCATATCCGTG	This study	N/A
Recombinant DNA		
pBabe-IR-A-GFP	Choi et al. ⁷⁷	N/A
		(Continued on payt or



Continued		
REAGENT or RESOURCE	SOURCE	IDENTIFIER
Lenti-CRISPR-Blasticidin-mouse IGF1R	This paper	N/A
Lenti-CRISPR-Blasticidin-human-IGF1R	This paper	N/A
entiCRISPR vector	Sanjana et al. ⁷⁸	Addgene, Cat#52962
sPAX2	Didier Trono	Addgene, Cat#12260
MD2.G	Didier Trono	Addgene, Cat#12259
DET29b(+)	GenScript	N/A
DEZT-BM	Morales-Perez et al. ⁷⁹	Addgene, Cat#74099
DEZT-BM-hIR-A-Y960F, S962A, D1120N, R1333A, I1334A, L1335A, L1337A-3C- Tsi3-His	Uchikawa et al. ¹⁸	N/A
EZT-BM-mIR-A-Y962F, D1122N	Li et al. ²⁰	N/A
oCS2-human IR-A-myc	Uchikawa et al. ¹⁸	N/A
CS2-human IR-B-myc	An et al. ¹⁹	N/A
oCS2-human IR-A-F64A-myc	Park et al. ³⁵	N/A
oCS2-human IR-A-F88A-myc	This paper	N/A
oCS2-human IR-A-F89A-myc	This paper	N/A
CS2-human IR-A-F96A-myc	Park et al. ³⁵	N/A
CS2-human IR-A-F64A/F96A-myc	This paper	N/A
CS2-human IR-A-F88A/F89A-myc	This paper	N/A
CS2-human IR-A-K484E/L552A-myc	Uchikawa et al. ¹⁸	N/A
CS2-human IR-A-R345A-myc	Park et al. ³⁵	N/A
CS2-human IR-A-R14W-myc	Park et al. ³⁵	N/A
CS2-human IR-A-D707A-myc	Park et al. ³⁵	N/A
oCS2-human IR-A-N15K-myc	Park et al. ³⁵	N/A
oCS2-human IR-A-D496K-myc	Park et al. ³⁵	N/A
Software and algorithms		
GraphPad Prism 10	Dotmatics	https://www.graphpad.com/
Adobe Illustrator	Adobe	https://www.adobe.com/products/ illustrator.html#modal-hash
FlowJo	BD Life Sciences	https://www.flowjo.com/flowjo/overview
PatchDock	Duhovny et al. ⁸⁰	https://www.cs.tau.ac.il/~ppdock/ PatchDock/
Rosetta	Leman et al. ⁸¹	https://rosettacommons.org/software/
DeepAccNet pLDDT	Hiranuma et al. ³³	https://github.com/hiranumn/DeepAccNe
ProteinMPNN	Dauparas et al. ⁸²	https://github.com/dauparas/ ProteinMPNN
AlphaFold 2 (AF2)	Jumper et al. ⁸³	https://www.alphafold.ebi.ac.uk/
Motioncor2 program (version 1.2)	Zheng et al. ⁸⁴	https://github.com/singleparticle/ MotionCor2
RELION 4.0	Zivanov et al. ⁸⁵	https://relion.readthedocs.io/en/release-20/index.html
Coot 0.98	Emsley et al. ⁸⁶	https://www2.mrc-lmb.cam.ac.uk/ personal/pemsley/coot/
Phenix 1.18	Adams et al. ⁸⁷	https://www.phenix-online.org/
Molprobity	Phenix validation tool set	https://phenix-online.org/documentation/reference/molprobity_tool.html
	Pettersen et al. ⁸⁸	https://www.cgl.ucsf.edu/chimera/
ChimeraX 1.7	Pettersen et al.	Tittps://www.cgi.ucsi.edu/chimera/

Molecular Cell

Article



Continued		
REAGENT or RESOURCE	SOURCE	IDENTIFIER
Superose 6 increase 3.2/300 analytical size-exclusion column	Cytiva	Cat#29091598
glow-discharged Quantifoil R1.2/1.3 300-mesh gold holey carbon grids	Quantifoil, Micro Tools GmbH, Germany	Cat#X-101-Au300
Nickel NTA beads	Qiagen	Cat#30210
Superdex 75 Increase 10/300GL columns	Cytiva	Cat#29148721

EXPERIMENTAL MODEL AND STUDY PARTICIPANT DETAILS

Mouse strains and Husbandry

Animal work described in this manuscript has been approved and conducted under the oversight of the Columbia University Institutional Animal Care and Use Committee. Mice (C57BL/6J, Jackson Laboratory, #000664) were fed a standard rodent chow (Lab diet, #5053) or high-fat diet (HFD) (D12492; Research Diets). All animals were maintained in a specific antigen-free barrier facility (temperature, 20-26 °C; humidity, 30-70%) with 12 h light/dark cycles (6 a.m. on and 6 p.m. off). Two to three-month-old male mice were used in this study.

Cell lines

293FT

293FT (Invitrogen, #R70007) were cultured in high-glucose Dulbecco's modified Eagle's medium (DMEM) supplemented with 10% (v/v) fetal bovine serum (FBS), 2 mM L-glutamine, and 1% (v/v) penicillin/streptomycin and maintained in monolayer culture at 37 °C and 5% CO₂ incubator.

Brown preadipocytes

IR and IGF1R double knockout brown preadipocytes expressing only human IR-B (DKO-IR-B) or mouse IR-A (DKO-IR-A) were kindly provided by Dr. Ronald Kahn. ⁸⁹ Cells were cultured in high-glucose Dulbecco's modified Eagle's medium (DMEM) supplemented with 10% (v/v) fetal bovine serum (FBS), 2 mM L-glutamine, and 1% (v/v) penicillin/streptomycin and maintained in monolayer culture at 37 °C and 5% CO₂ incubator.

C2C12

C2C12 (ATCC, CRL-1722) cells were cultured in high-glucose DMEM supplemented with 10% (v/v) FBS, 2 mM L-glutamine, and 1% penicillin/streptomycin and maintained in monolayer culture at 37 °C and 5% CO2 incubator.

MCF7

MCF7 (ATCC, HTB-22) cells were cultured in high-glucose DMEM supplemented with 10% (v/v) FBS, 2 mM L-glutamine, and 1% penicillin/streptomycin and maintained in monolayer culture at 37 °C and 5% CO2 incubator.

FreeStyle™293-F

FreeStyle™293-F (Invitrogen, R79007) were cultured in FreeStyle™293 Expression Medium and maintained in an orbital shaker at 37 °C and 5% CO₂ incubator.

Spodoptera frugiperda (SF9)

SF9 (Invitrogen, 11496015) were cultured in SF900 II SFM (Gibco) at 27 °C with orbital shaking at 120 rpm.

Cell line validation

Following passage of an aliquot of each cell line for up to three weeks, a fresh batch of cells were thawed and propagated. There were no signs of mycoplasma contamination.

Yeast and Bacteria strains

EBY-100 yeast cells (ATCC, MYA-4941) were cultured in CTUG medium (MP Biomedicals, Cat# 114520512-CF) at 30 °C. *E. coli* Stbl3 (Invitrogen, Cat# C737303), DH10Bac (Thermo Fisher Scientific, Cat# 10361012), and HST08 (Takara Bio, Cat# 636763) were cultured in LB broth at 37 °C with shaking at 250 rpm for 14 h. BL21(DE3) cells (NEB, Cat# C2527I-81) were cultured in TBII medium (MP Biomedicals) at 37 °C with shaking at 250 rpm. Conditions for protein expression induction are described in the respective subsections of the STAR Methods.

METHOD DETAILS

Computational design of the IR site-2 binders

The computational design method was using the method previously described. ²⁶ In brief, IR structure 6PXV was downloaded from Protein Data Bank and relaxed by Rosetta guided by experimental design-guided relaxation. The F1 domain (residue 467-590) was extracted as the targeting domain and the insulin binding side was selected as the targeting interface. For each residue of the selected interface, Rotamer Interaction Field (RIF) was generated. Later, mini-protein scaffold set, composed of 3 helical, 4 helical





and ferredoxin scaffolds, were used to search for global shape complementarity with PatchDock. The docked scaffolds were then sequenced sequence-optimized using Rosetta FastDesign and evaluated by DeepAccNet³³ pLDDT and Rosetta Metrics including ddG, contact patch, and contact molecular surface.²⁶ A total of 11,280 oligos encoding designed site 2 binders passed the filters.

Computational design of the linked binders

Amino acid residues not involved in interacting with IR were redesigned to improve the solubility of S2-F1-S1 using the deep learning-based sequence design method ProteinMPNN⁸² (see also: https://github.com/dauparas/ProteinMPNN/blob/main/examples/submit_example_4.sh).

To generate Rigidly-linked IR binders, we aligned the design models of S1B/L1 and S2B/F1 to the S2-F1-S1/IR complex as the starting point. The first helix of S1B (Up to residue 3) and the last helix of S2B (Residue 54 onwards) were rebuilt by RFdiffusion²⁸ to link the L1- and F1-binding interfaces. Surface residues near the diffused regions were masked and redesigned using ProteinMPNN⁸² along with the newly built regions. 32 sequences were generated for each backbone. Then, the designs were predicted by AlphaFold 2 (AF2), relaxed and scored by Rosetta. The top 28 designs with the highest AF2 pLDDT and lowest RMSD to design were selected for experimental characterization. Sequence optimization was further performed to improve solubility of the Rigidly-linked IR binders.

Yeast surface display screening for IR site 2 binders with FACS

The yeast surface display screening was performed using the protocol as previously described. ²⁶ Briefly, DNAs encoding the minibinder sequences were transformed into EBY-100 yeast strains. The yeast cells were induced in SGCAA medium. After washing with FACS-buffer (PBS, Fisher Scientific, supplemented with 1% w/v bovine serum albumin, Sigma Aldrich), the cells were incubated with 1uM biotinylated IR F1 domain together with streptavidin–phycoerythrin (SAPE, ThermoFisher, 1:100) and anti-c-Myc fluorescein isothiocyanate (FITC, Miltenyi Biotech, 6.8:100) for 60 min. After washing twice with FACS buffer, the yeast cells were then resuspended in the buffer and screened via FACS. Only cells with PE and FITC double-positive signals were sorted for next-round screening. After another round of enrichment, the cells were titrated with biotinylated IR F1 domain at 100 nM, 10 nM and 1 nM for 60 min, washed, and further stained with both streptavidin–phycoerythrin (SAPE, ThermoFisher) and anti-c-Myc fluorescein isothiocyanate (FITC, Miltenyi Biotech) at 1:100 ratio for 30 min. After washing twice with FACS buffer, the yeast cells at different concentrations were sorted individually via FACS and regrown for 2 days. Next, the cells from each subpool were lysed and their sequences were determined by next-generation sequencing.

Protein binder expression and purification

Synthetic genes encoding designed proteins were purchased from GenScript or Integrated DNA Technologies (IDT) in the pET29b expression vector or as eBlocks (IDT) and cloned into customized expression vectors 90 using Golden Gate cloning. A His6x tag was included either at the N-terminus or the C-terminus as part of the expression vector. Proteins were expressed using autoinducing TBII media (Mpbio) supplemented with 50x5052 and 20 mM MgSO₄ in BL21 DE3 *E.coli* cells. Proteins were expressed under antibiotic selection at 25 $^{\circ}$ C overnight after initial growth for 6–8 h at 37 $^{\circ}$ C. Cells were harvested by centrifugation at 4000x g and resuspended in lysis buffer (20 mM Tris, 300 mM NaCl, 5 mM imidazole, pH 8.0) containing protease inhibitors (Thermo Scientific) and Bovine pancreas DNasel (Sigma-Aldrich) before lysis by sonication.

Proteins were purified by Immobilized Metal Affinity Chromatography (IMAC). Cleared lysates were incubated with 0.1-0.5 mL nickel NTA beads (Qiagen) for 20-40 minutes before washing beads with 5-10 column volumes of lysis buffer, 5-10 column volumes of wash buffer (20 mM Tris, 300 mM NaCl, 30 mM imidazole, pH 8.0). Proteins were eluted with 1-4 mL of elution buffer (20 mM Tris, 300 mM NaCl, 300 mM imidazole, pH 8.0). All protein preparations were as a final step polished using size exclusion chromatography (SEC) on Superdex 75 Increase 10/300GL columns (Cytiva) using PBS buffer (Fisher Scientific). SDS-PAGE and LC/MS were used to verify peak fractions. Proteins were concentrated to concentrations between 0.5-10 mg/mL and stored at room temperature or flash frozen in liquid nitrogen for storage at -80 °C. Thawing of flash-frozen aliquots was done at room temperature. All purification steps from IMAC were performed at ambient room temperature.

Biolayer interferometry (BLI)

The BLI experiments were performed on an OctetRED96 BLI system (ForteBio) at room temperature in HBS-EP buffer (Cytiva Life Sciences) supplemented with 0.2 % w/v bovine serum albumin (BSA, SigmaAldrich). Prior to measurements, streptavidin-coated biosensors were first equilibrated for at least 10 min in the assay buffer. Biotinylated target proteins (IR F1 domain, IR extracellular domain (ECD) (ACROBIOsystems INR-H82E6), IGF1R ECD (ACROBIOsystems IGR-H82E3)) were immobilized onto the biosensors by dipping them into a solution with 100 nM protein until the loading signal reaches 0.5 - 1 nm. Association and dissociation of the analytes were monitored by dipping biosensors in the solutions containing analytes at various concentrations for 300s followed by dipping the biosensors in fresh buffer for 300 s. Experiments were performed at 25 °C while rotating at 1000 rpm. Global kinetic or steady-state fits were performed on buffer-subtracted data using the manufacturer's software (Data Analysis 12.1) assuming a 1:1 binding model.

Molecular Cell Article



Circular Dichroism Spectroscopy

CD spectra were recorded in a 1 mm path length cuvette at a protein concentration between 0.3-0.5 mg/mL on a J-1500 instrument (Jasco). For temperature melts, data were recorded at 222 nm between 25 and 95 °C every 2 °C, and wavelength scans between 190 and 260 nm at 10 °C intervals starting from 25 °C. Experiments were performed in 10 mM sodium phosphate buffer (pH 7.4), 50 mM NaCl. The high tension (HT) voltage was monitored according to the manufacturer's recommendation to ensure optimal signal-tonoise ratio for the wavelengths of interest.

Protein expression and purification for cryo-EM

For structural studies, the short isoform of human insulin receptor (hIR) or mouse insulin receptor (mIR, sharing 94% sequence identity with hIR) were cloned into pEZT-BM expression vectors by Gibson assembly (NEBuilder HiFi DNA Assembly Cloning kit, New England Biolabs), as described previously. ^{18–20} To improve expression and protein behavior, seven mutations (Y960F, S962A, D1120N, R1333A, L1335A, L1337A: amino acid numbering of short isoform of mature hIR) were introduced to hIR, and two mutations (Y962F and D1122N, amino acid numbering of short isoform of mIR without signal peptide) were introduced to mIR. The human rhinovirus 3 C recognition site (3C), affinity purification tag Tsi3 (T6SS secreted immunity protein three from *Pseudomonas aeruginosa*) and His₈ tag were fused to the C-terminus of both proteins.

The expression and purification of hIR and mIR were performed following previously described protocols with minor modifications. ^{18–20} Briefly, the plasmids were transformed to *Escherichia coli* strain DH10Bac to produce bacmid DNA. Recombinant baculovirus was generated by transfecting Sf9 cells with bacmid DNA using Cellfectin reagent (Gibco). hIR or mIR proteins were expressed in FreeStyle 293-F cells by infecting the cells with the virus at 1:10 (virus: cell, v/v) ratio. Six hours after infection, 8 mM sodium butyrate was added to boost protein expression. Cells were cultured in a shaking incubator supplemented with 8% CO₂ for 48–60 h at 30 °C before harvesting.

The cells were resuspended in lysis buffer containing 40 mM Tris-HCl pH 7.5, 400 mM NaCl (Buffer A) with Protease Inhibitor Cocktail (Roche) and lysed by using a French Press cell disruptor. The membrane fraction was obtained by ultracentrifugation of the cell lysate for 1 h at 100,000 g at 4 °C. To extract the protein from the membrane fraction, Dodecyl maltoside (DDM, Anatrace) was added to a final concentration of 1% (m/v) with stirring overnight. The supernatant containing the solubilized protein was obtained by ultracentrifugation for 1 h at 100,000 g at 4 °C. The supernatant was added with 2 mM CaCl₂ and Tse3 protein-conjugated Sepharose resin (GE Healthcare) and incubated at 4 °C for 1 h before being loaded onto a column by gravity flow. The resin was subsequently washed with 40 column volumes (CV) of buffer containing 40 mM Tris-HCl pH 7.5, 400 mM NaCl, 2 mM CaCl₂, 5% glycerol (v/v), 0.05% DDM (m/v) (Buffer B) and eluted by HRV-3C protease cleavage at 4 °C overnight. The protein was then concentrated using a 100 kDa cutoff concentrator (Millipore), loaded onto a Superose 6 increase 10/300 GL size-exclusion column (Cytiva), and eluted with buffer containing 20 mM HEPES pH 7.4, 150 mM NaCl and 0.03% DDM (Buffer C). The dimer fractions of mIR or hIR proteins were identified by SDS-PAGE and pooled.

To make Insulin/S2B/mIR complex for cryo-EM analyses, commercial insulin (I2643, Sigma) and site-2 binder (S2B) were mixed with purified mIR at a molar ratio of 4:4:1 (insulin: S2B: mIR). Given the high binding affinity of S2B ($K_D \approx 2$ nM) for the FnIII-1 domain of IR, compared to the micromolar affinity of insulin, we hypothesized that S2B would outcompete insulin at IR site-2. To make RF-405/hIR, S2-F1-S1/hIR, and S1-F8-S2/hIR complexes, RF-405, S2-F1-S1, S1-F8-S2 binders were mixed with purified hIR at a molar ratio of 4:1 (binder: hIR). After incubation for 30 min, the protein mixtures were concentrated to 6-8 mg mI⁻¹ using 100 kDa cutoff concentrators (Millipore) and subject to cryo-EM grid preparation immediately. All purification and following steps were performed at 4 °C or on ice.

For analytical size-exclusion chromatography of S2-F1-S1/hIR and RF-405/hIR complexes, S2-F1-S1 or RF-405 were added to hIR at a molar ratio of 4:1 (binder: hIR). After incubation for 30 min, the protein mixtures were then loaded onto a Superose 6 increase 3.2/300 analytical size-exclusion column (Cytiva) and eluted with Buffer C.

Cryo-EM data collection and image processing

EM data acquisition, image processing, and model building, and refinement were performed following previous protocols with some modifications. ^{18–20,35} The samples of IR in complex with insulin/S2B, RF-405, or S2-F1-S1 were applied to glow-discharged Quantifoil R1.2/1.3 300-mesh gold holey carbon grids (Quantifoil, Micro Tools GmbH, Germany). Grids were blotted under 100% humidity at 4 °C and plung-frozen in liquid ethane using a Mark IV Vitrobot (Thermo Fisher Scientific). Micrographs were collected in the counting mode on either Glacios or Titan Krios microscopes (Thermo Fisher Scientific) with either Falcon4 (Thermo Fisher Scientific) or K3 Summit direct electron detectors (Gatan). The nominal magnification and pixel size of each data set are summarized in Table 1.

Motion-correction and dose-weighting of the micrographs were carried out using the Motioncor2 program (version 1.2). ³⁴ GCTF 1.06 was used for CTF correction. ⁹¹ Template-based particle picking was carried out using the autopick tool in RELION 4.0. ^{91,92} Particles were cleaned up with multiple rounds of 2D and 3D classification in RELION. Good particles were selected and subjected to 3D refinement with C2 symmetry. The exact procedures are summarized in supplementary figures. The initial mode for 3D classification and refinement was generated using the SGD method in RELION. The refined maps were further improved by using Bayesian polishing and CTF refinement at the final stage. The Fourier Shell Correlation (FSC) 0.143 criterion was used for estimating the resolution of the maps. Local resolution was calculated in RELION.





Model building and refinement

To build the atomic models of the IR structures with different binders bound, the published model of each domain of human IR (PDB: 6PXV) and the predicted models of S2B, RF-405 or S2-F1-S1 using AlphaFold2⁸³ were docked into the cryo-EM maps as rigid-body. The models were adjusted manually in Coot 0.98.⁸⁶ The models were refined using the real-space refinement module in Phenix 1.18.⁹³ Model quality was checked using Molprobity as a part of the Phenix validation tool set.⁹⁴ Model statistics are summarized in Table 1. Structural figures were rendered in ChimeraX 1.7.^{88,95}

Transfection and viral infection

Plasmid transfections into 293FT cells were performed with LipofectamineTM 2000 (Invitrogen). To generate C2C12 cells expressing human IR-A, 293FT cells were transfected with pBabe-human IR-A-GFP with packaging vectors as described earlier with some modification. To Virus was collected at 2- and 3-days after transfection and concentrated with homemade virus concentrator. C2C12 cells were infected with concentrated virus and polybrene (4 ug/ml). Cells were selected with 2 mg/ml of puromycin at 3 days after infection and sorted using FACS sorter (Sony Ma900). To generate IGF1R knockout C2C12 cells expressing human IR-A (C2C12-IR), lentiviruses were packaged in 293FT cells by transfecting the cells with lentiCRISPR vector, psPAX2 (Addgene #12260), and pMD2.G (Addgene #12259). Viruses were collected at 2- and 3-days after transfection and concentrated. C2C12 cells expressing IR-A were infected with concentrated virus and polybrene (4 ug/ml). Cells were selected with blasticidin (10 mg/ml) for 3 weeks.

IR signaling assay

The IR signaling assay was performed as described earlier with some modification. ^{19,20,35,96} For IR mutants assay, 293FT cells were transfected with Myc-tagged IR mutants or WT. One day later, the cells were serum starved for 14-16 h. Serum-starved cells were treated with insulin (I2526, Sigma) or designed binders for 10 min. For binder validation, DKO-IR-A, DKO-IR-B, or C2C12-IR cells were used. Two days after seeding, the cells were serum starved for 6 h. Serum-starved cells were treated with insulin or designed binders for 10 min. To analyze antagonistic effects of binders, cells were serum starved for 4 h, treated with the indicated concentrations of binders for 1 h, and then treated for 10 min with insulin at the indicated concentrations.

After treatment, cells were incubated with cell lysis buffer B [50 mM Hepes pH 7.4, 150 mM NaCl, 10% (v/v) Glycerol, 1% (v/v) Triton X-100, 1 mM EDTA, 10 mM sodium fluoride, 2 mM sodium orthovanadate, 10 mM sodium pyrophosphate, 0.5 mM dithiothreitol (DTT), 2 mM phenylmethylsulfonyl fluoride (PMSF)] supplemented with cOmplete Protease Inhibitor Cocktail (Roche), PhosSTOP (Roche), and 25 U/ml turbo nuclease (Accelagen) on ice for 1 h. After centrifugation at 18,213 g at 4°C for 20 min, cell lysate samples were made with SDS-PAGE protein loading buffer. Cell lysates were analyzed by SDS-PAGE and Western blotting. Anti-IR-pY1150/ 1151 (1:2000, 19H7, Cell signaling; labeled as pY IR (or pY IGF1R), #3024), anti-IR-pY1146 (1:1000, D6D5L, Cell signaling, #80732S), anti-IR-pY960 (1:1000, Invitrogen, #44-800G), anti-IR-Y1316 (1:1000, Invitrogen, #44-807G), anti-IR-Y1322 (1:1000, Invitrogen, #44-809G), anti-IRS1 (1:500, BD bioscience, #611394), anti-pY608 IRS1 (1:1000, Millipore, #09-432), anti-SHC (1:500, Santa Cruz, PG-797, sc-697), anti-pY239/240 SHC (1:500, Cell signaling, #2434), anti-Myc (1:2000; 9E10, Roche; labeled as IR, #11667149001), anti-IR (1:500; CT3, Santa Cruz, sc-57342), anti-AKT (WB, 1:2000; 40D4, #2920), anti-pS473 AKT (WB, 1:2000; D9E, #4060), anti-ERK1/2 (WB, 1:2000; L34F12, #4696), and anti-pERK1/2 (WB, 1:2000; 197G2, #4377) were used as primary antibodies. For quantitative Western blots, anti-rabbit immunoglobulin G (IgG) (H+L) (Dylight 800 conjugates, #5151) and anti-mouse IgG (H+L) (Dylight 680 conjugates, #5151) and IgG (H+L) (Dylight 680 conjugates, H+L) (Dylight 680 co jugates, #5470) (Cell signaling) were used as secondary antibodies. The membranes were scanned with the Odyssey Infrared Imaging System (LI-COR, Lincoln, NE). Levels of phosphorylation were normalized to total protein levels and shown as intensities relative to that in WT insulin alone (Figures 1J, 3E, 3F, and 4C-4H). Levels of IR autophosphorylation were normalized to total IR levels and shown as intensities relative to that in WT IR in insulin-treated cells (Figures 6C, 6E, and 6F).

IR signaling analysis in vivo

IR signaling *in vivo* analysis was performed as described earlier with some modifications. ^{20,35,77,97} 2-3-months-old male mice were fasted overnight. Following anesthesia, mice were injected with 6 nmol Humulin (Eli Lilly) or 9 nmol designed agonists per mouse via inferior vena cava. Livers and skeletal muscle were removed at 5 min and 10 min after injection, respectively. Tissues were homogenized in cell lysis buffer B supplemented with cOmplete Protease Inhibitor Cocktail (Roche), PhosSTOP (Sigma), and 25 U/ml turbo nuclease (Accelagen), homogenized with FisherbrandTM Bead Mill homogenizer, and then incubated on ice for 1hr. After centrifuge at 20,817 g at 4°C for 30 min, the concentrations of cell lysate were measured using Micro BCA Protein Assay Kit (Thermo Scientific). The lysates were then analyzed by quantitative western blotting (Li-COR, Lincoln, NE).

Primary mouse hepatocytes isolation

Mouse primary hepatocytes were isolated from 2- to 3-month-old male mice using a standard two-step collagenase perfusion procedure. 35,77 Briefly, livers were perfused via the portal vein with prewarmed perfusion buffer (Gibco BRL 17701-038), followed by digestion buffer containing collagenase (Gibco BRL 17703-034). The excised liver was gently dissociated, and hepatocytes were filtered, washed, and pelleted by 50 g for 3 min at 4°C. Isolated hepatocytes were resuspended with attached medium [Williams' Medium E supplemented with 5% (v/v) FBS, 10 nM insulin, 10 nM dexamethasone, and 1% penicillin/streptomycin] and plated

Molecular Cell Article



on collagen (Sigma, C3867)-coated dishes. After 4 h, the medium was changed to serum free low-glucose DMEM supplemented with 1% penicillin/streptomycin. After 14-16 h, the cells were treated with insulin to analyze IR signaling and IR endocytosis.

Cell surface biotinylation and streptavidin pulldown

Cell Surface labeling was performed as previously described with some modifications. Primary mouse hepatocytes were treated with 100 nM ligands for 30 min. Cells were washed with in cold PBS, pH 8.0 (Corning, 21-030-CM) and incubated in 0.5 mg/ml EZ-link™Sulfo-NHS-LC-Biotin (Thermo Fisher, 21335) dissolved in PBS, pH 8.0 on ice for 10 min. The labeling reaction was quenched in 50 mM glycine in two sequential 10 min incubations on ice. Cells were incubated with RIPA buffer (Thermo Fisher, 89901) supplemented with Halt Protease & Phosphatase inhibitor cocktail (Thermo Fisher, 78442) on ice for 1 h. After centrifugation at 18,213 g at 4°C for 20 min, the supernatant was taken for streptavidin pulldown. Lysates were incubated with streptavidin magnetic beads (Thermo Fisher, 88817) overnight and washed 3 times with RIPA buffer. Beads were eluted with SDS sample buffers and samples were analyzed by SDS-PAGE and Western blotting. Anti-IR (1:500; CT3, Santa Cruz, sc-57342), anti-beta catenin (1:1000, D10A8, Cell signaling, #8480), anti-Actin (1:1000, C4, Santa Cruz, #sc-47778).

Insulin tolerance test

Mice were fasted for 2h (healthy mice) or 5 h (diet-induced obese mice) and their blood glucose levels (T=0) were measured with tail bleeding (Contour Next). Mice were then injected intraperitoneally with PBS, Humulin or designed agonists. Their blood glucose levels at the indicated time points after injection were measured with tail bleeding.

Cell proliferation assay

C2C12-IR, MCF7 wild-type, and MCF7 IGF1R knockout cells were seeded in 0.1 million cells per 35 mm cell culture dish. One day later, cells were serum starved for 24 h and then treated for 24 h with indicated concentrations of binders in the presence or absence of insulin. One day later, cells were pulsed with 10 µM bromodeoxyuridine (BrdU) for 2 h, then fixed with 70% cold ethanol. The fixed cells were washed with FACS blocking solution (0.02% Triton X-100 and 1% BSA in PBS), denatured with 3N HCl for 30 min, neutralized with phosphate/citrate buffer for 10 min, and then washed three times with the FACS blocking solution. 10uL of FITC-anti-BrdU antibody (BD, #556028) was added to each sample and incubated at RT for 2.5 h. cells were washed with the FACS blocking solution and stained with propidium iodide (BD, #550825). Cells were analyzed using BD FACSCanto II from the Flow Cytometry Core of the Columbia Center for Translational Immunology (CCTI) and Herbert Irving Comprehensive Cancer Center (HICCC). Data was processed with FlowJo.

QUANTIFICATION AND STATISTICAL ANALYSIS

Prism 10 was used for the generation of graphs and for statistical analyses. Results are presented as mean \pm s.d. or mean \pm s.e.m. Two-tailed unpaired t tests were used for pairwise significance analysis. For dose-response curve, the relative intensity signals were fitted to a four-parameter sigmoidal concentration-response curve, from which the pEC $_{50}$ values (negative logarithmic values of half-maximum effective concentration (EC $_{50}$) values) were used to calculate the mean and s.e.m. Log-transformed EC50 values were analyzed by Extra sum-of-squares F Test in Prism, between insulin and designed agonists. Two-way ANOVA followed by Tukey's multiple comparisons tests were used in case of more than two factors' comparisons. No power analysis for sample sizes was performed. Randomization and blinding methods were not used, and data were analyzed after the completion of all data collection in each experiment.